Coupled electronic and nuclear dynamics at interfaces of artificial photosynthesis devices

Haas, T. de

Chapter 4: Hybrid-DFT Molecular Dynamics Simulations of Photocatalytic Water Oxidation in a [Ru-bda]–Dye Complex

The catalytic cycle of a dye-catalyst supramolecular complex for water oxidation is investigated using DFT-MD simulations.

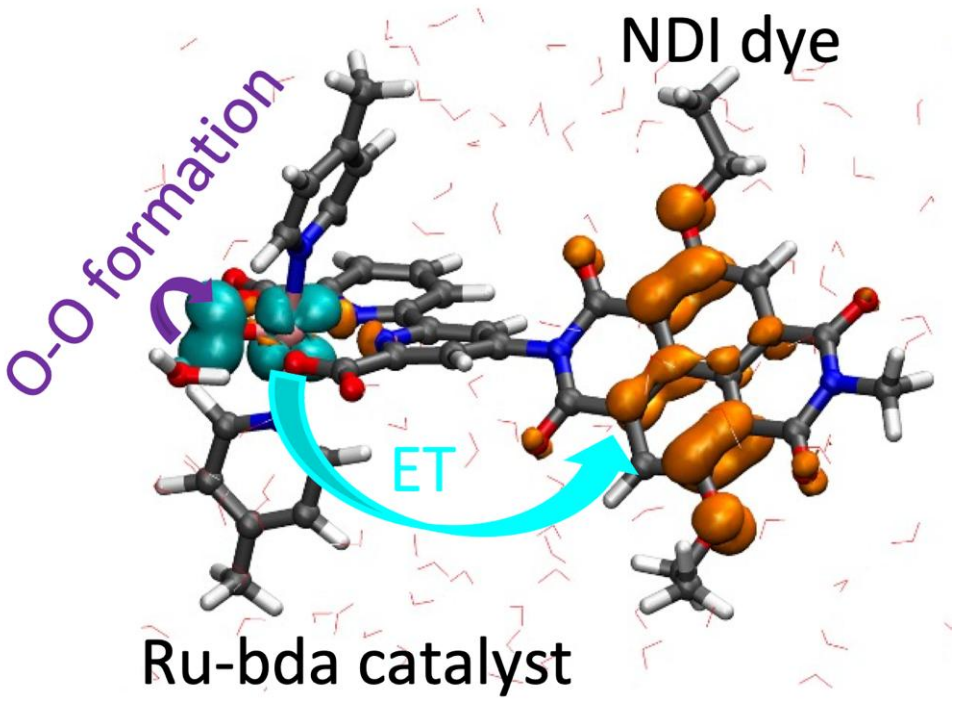

This chapter is based on:

T. de Haas, D. Calvani, A. Zaaruolo, T. de Jong, J. Rutgers, B. Kreupeling, H.J.M. de Groot, F. Buda. Hybrid-DFT Molecular Dynamics Simulations of Photocatalytic Water Oxidation in a [Ru-bda]–Dye Complex. *J. Phys. Chem. C.* **2024**, *128* (47), 20093-20103.

4.1 Abstract

In the past decade, Ru-bda (bda = 2,2'-bipyridine-6,6'-dicarboxylic acid) complexes have emerged as extremely effective water oxidation catalysts, rendering them a potential candidate for incorporation into dye-sensitized photoelectrochemical cells. However, the performance of these catalysts declines dramatically when anchored to a photoanode surface due to their catalytic mechanism involving the interaction of two metal centers (I2M). This reduced performance prompts an investigation into the catalytic cycle following an alternative mechanism in which the O-O bond is formed through a water nucleophilic attack (WNA). In this work, we have performed hybrid-DFT based molecular dynamics simulations of the rate-determining O-O bond formation following the WNA mechanism in a [Ru-bda]-dye dyad model in explicit water solvation. In addition, our study probes oxygen dissociation from the Ru^{III}-O_2 intermediate, and the equilibrium dynamics of the low-valent Ru^{III}-bda intermediate. Our simulations demonstrate that including a fraction of exact Hartree-Fock exchange impacts the electron and hole localizations in the catalyst-dye complex, which can in specific instances affect the dynamics of the system. This study contributes to a fundamental understanding of water oxidation catalysis with the Ru-bda catalyst family and highlights the relevance of modeling catalytic processes at the hybrid-DFT level.

4.2 Introduction

In view of an escalating global climate crisis, harnessing solar energy for fuel production stands as a promising endeavor, offering a potential route towards the mitigation of greenhouse gas emissions.[1–4] Dye-sensitized photoelectrochemical cells (DS-PEC) are devices that use sunlight to convert water and other abundant chemical resources into solar fuels.[5,6] Typically, a DS-PEC contains two compartments. At the anode compartment, four photons are used to oxidize two molecules of water into four protons, four electrons, and one molecule of oxygen (O_2). At the cathode of the cell, the acquired reduction potential and the protons are used to generate molecular hydrogen or reduce a carbon-based feedstock into a denser energy carrier such as ethanol or ethylene.[7]

At the anode of the DS-PEC, three chemical components are responsible for the water-splitting process: the semiconductor surface, a water oxidation catalyst (WOC) and a dye molecule. Photon absorption by a dye molecule initiates a charge separation process. The excited dye can donate an electron to the semiconductor surface, usually TiO_2, and inject a hole into the WOC. This last step provides the driving force for one of the proton-coupled electron transfer (PCET) steps that constitute the water oxidation catalytic cycle. In practice, many photo-responsive anodes are based on solid state materials with an activity which is often hampered by slow reaction kinetics and inefficient photoactivity of the semiconductors.[8] In contrast to solid state catalysts, specific molecular catalysts have been reported that perform at much lower overpotentials, in some cases even reaching higher activities than photosystem II.[9,10] In light of this, it becomes highly compelling to adopt a design wherein the catalyst and dye molecules are present in a homogeneous solution or co-deposited on the semiconductor surface. However, a major disadvantage of such approaches is that the charge recombination reaction, in which the oxidized dye is quenched by electron-hole recombination from the TiO_2 surface, becomes competitive with the hole-scavenging of the catalyst.[11] To overcome this issue, intermolecularly linked dye-catalyst complexes have been synthesized, either through covalent

interactions,[12,13] or through supramolecular assembly strategies.[11] In these photo-anodes, the interfacial electron transfer is typically very fast and the efficiency is proposed to be hampered by the chemical conversion rate of the catalyst.[14]

One class of water oxidation catalysts that has shown to be particularly promising was developed in the labs of Sun and Llobet.[9,15] This family of complexes employs a ruthenium center bearing a bda^{2-} (= 2,2'-bipyridine-6,6'-dicarboxylic acid) ligand in the equatorial plane and two monodentate pyridyl-type ligands on the axial positions. Because the Ru valence shell in the Ru^{II}-bda complex is completely occupied, the complex becomes catalytically active only after an initial oxidation to form a Ru^{III} species. The tetra-coordinated bda^{2-} backbone leads to a distorted octahedral environment around the ruthenium atom, leaving space for a water molecule to coordinate. However, whether that leads to a 7-coordinated environment around the Ru^{III} center remains a matter of debate, as the flexible bda^{2-} ligand has also been shown to be able to lower its coordination number, either by elongation of one of the equatorial Ru-$N_{bda^{2-}}$ bonds (k^3-O^2N^1 binding mode) or by elongation of the Ru-O_{COO^-} distance (k^3-O^1N^2 binding mode).[16–18] As the dynamic behavior of this low-valent complex in solution is still not entirely understood, a DFT-based Molecular Dynamics (DFT-MD) investigation of the coordination chemistry of this complex is desirable.

The Ru-bda family of catalysts typically performs the rate-limiting oxygen-oxygen bond-forming step through a bimolecular mechanism in which two Ru^V=O species couple to form a Ru^{IV}-O-O-Ru^{IV} complex that can eventually dissociate O_2.[9,19] This interaction of two metal (I2M) mechanism is postulated to be the major reason for a high catalytic activity of this catalyst class. As a result of its excellent performance, the Ru-bda catalyst has been used as a prototype to study water oxidation in systems where catalysts have been immobilized on surfaces, in supramolecular structures, and even in lipid bilayers and metal-organic frameworks.[20–24] It remains questionable, however, whether the high

performance of this catalyst is preserved once the intermolecular collision frequency is significantly reduced as a result of catalyst immobilization. A recent study has shown that after immobilization on TiO_2, the catalyst activity was quenched significantly, even though a second-order kinetics in the catalyst concentration was preserved.[22] This is particularly interesting, since under such conditions a different mechanism is typically expected to become dominant in ruthenium based catalysts.[25] In this alternative mechanism, the O-O bond is formed through a nucleophilic attack of a solvent water molecule on the high valent Ru^{V}=O, culminating in formation of the Ru^{IV}-O-OH intermediate (WNA pathway). After a fourth PCET step, a Ru^{III}-O_2 species could be formed, leading to dissociation of the dioxygen ligand to recover the initial catalyst. The amount of work published on the WNA mechanism is significantly less than that on the I2M mechanism in the Ru-bda family, and an in-depth investigation of this alternative catalytic cycle, as well as an estimation of the reaction barriers, is appropriate.

In this work, we performed DFT-MD simulations of all four, proton-coupled electron transfer steps of the WNA mechanism in a Ru-bda catalyst, covalently bound to a naphthalene diimide (NDI) dye in explicit water solvation. Including the electron-accepting NDI and the proton-accepting water environment explicitly, allowed us to study the proton and electron transfer events during the simulation. This work addresses two questions regarding the catalytic cycle of the Ru-bda^{2-} catalyst class. First, we aim to establish a comprehensive picture of the equilibrium dynamics of the low-valent Ru^{III} intermediate, which is a debated topic in literature. Second, we evaluate the suitability of this catalyst for DS-PEC devices. Specifically, we determine the barrier for O-O bond formation following a nucleophilic attack of a water molecule on the Ru^{V}=O intermediate, and we investigate the O_2 dissociation from the catalyst after the final PCET step.

Over the past three decades, density functional theory (DFT) based on the generalized gradient approximation (GGA) has become the workhorse of DFT-MD due to its numerical efficiency and accurate predictive power when it comes

to thermodynamic properties and structures. Despite its extensive use in modeling molecular water oxidation catalysis,[26–31] GGA-DFT is known to suffer from a large self-interaction error, which leads to over-delocalized charge distributions.[32–34] This has been clearly demonstrated for Cl^- ions in water and ineffective hole-localizations in materials and surfaces.[33,35] By applying the Auxiliary Density Matrix Method (ADMM),[36] we could afford to include exact exchange and perform simulations at the hybrid-DFT level, which can correct the over-delocalization errors.[35] Next to addressing the previously posed questions regarding the Ru-bda catalyst, this study also aims to assess the effects of including a fraction of screened-Hartree-Fock exchange in the description of the electronic structure.

The applied computational methodologies are described in section 4.3. The performed DFT-based molecular dynamics simulations of PCET reactions are discussed in detail in paragraphs 4.4.1 – 4.4.4. Section 4.4.1 describes the equilibrium dynamics of the low-valent Ru^{III}-bda intermediate. Section 4.4.2 deals with the enhanced sampling simulations of the O-O bond formation step, while section 4.4.3 investigates the oxygen dissociation from the catalyst after the fourth PCET reaction. The conclusions of this paper are presented in section 4.5.

4.3 Computational methods

The optimized initial structure of the dye-$[Ru(bda)(pic)(OH)]^+$ complex was already obtained in a previous computational work.[37] The complex was placed in a cubic box with periodic boundary conditions. 199 explicit water molecules were added using the PACKMOL[38] builder tool in the AMS2022.102 package by SCM.[39] Subsequently, GROMACS was used to perform classical molecular dynamics (MD) simulations in which the water solvent molecules were equilibrated.[40] In these simulations, the water molecules were modeled with the TIP-3P force field, while the LigParGen tool was used to generate a set of OPLS-AA parameters for the non-metal atoms in the WOC-dye complex.[41–45] As this

tool does not allow for metal parameter optimization, the ruthenium atom was replaced with a seven-coordinated sulfur atom during the optimization run, and the ε and σ Van der Waals parameters for ruthenium were obtained from Bernardes *et al.* (the employed OPLS-AA force field parameters can be found attached to the publication by de Haas *et al.*).[46] Partial charges for all atoms of the WOC-dye complex were obtained from the Mulliken charges calculated at the B3LYP-D3(BJ)/TZP level on the optimized geometry.[37] In these classical MD equilibration runs, the atoms in the WOC-dye complex were kept at fixed positions. After an initial geometry relaxation, 5 ns of NVT ensemble simulation followed by 10 ns of NPT ensemble simulation were performed, each with a 2 fs timestep. These simulations employed the Berendsen thermostat and the Parrinello-Rahman barostat, respectively.[47–49] The volume equilibration yielded a cubic box with a side length of 20.343 Å and the temperature was stable around 300 K (see Appendix, Figure 4A.1). This system was subsequently used as the input for the DFT-MD simulations. Before the production runs, additional NVT simulations were performed at the DFT-MD level to equilibrate the whole system including the WOC-dye complex at 300 K. These calculations were performed with the Canonical Sampling Through Velocity Rescaling (CSVR) thermostat with a time constant set to 20 fs. The production runs were performed with a time constant of 150 fs. The time evolution of the temperatures of these runs is provided in the Appendix, Figure 4A.2.

All Kohn-Sham density functional theory simulations were carried out with the Quickstep routine in the CP2K8.2 software package.[50] All pure-DFT calculations were performed with the PBE exchange-correlation functional, while hybrid-DFT simulations were performed at the B3LYP level. All simulations included Grimme's pairwise additive D3 dispersion corrections with a cut-off of 22 Å and grid-smoothening.[51–54] The valence electrons for ruthenium were modelled with the DZVP-MOLOPT-SR-GTH basis set, while all other elements were modelled with the DZVP-MOLOPT-GTH basis.[55] The core electrons were described using the GTH pseudopotentials optimized for the PBE functional.[56–58] A value of 280

Ry was used as cut-off for the auxiliary plane wave (PW) basis. The PW integration was performed on a 5-layer multi-grid with the relative cut-off parameter set to 40 Ry. The orbital transformation (OT) method was used for the SCF procedure, employing a preconditioner based on diagonalization and inversion of the complete $\mathbf{H} - \epsilon^0\mathbf{S}$ matrix in conjunction with the conjugated gradient minimizer.[59] The convergence accuracy was set to 10^{-6} Hartree, which was found to conserve the total energy in the molecular dynamics simulations. Hybrid-DFT calculations were performed with the B3LYP functional containing a 0.2 fraction of screened Hartree-Fock exchange (HFX).[60–63] The HFX part was computed in an auxiliary density matrix using the AUX_FIT cFIT11 basis for ruthenium and the AUX_FIT cFIT3 basis for all other elements.[36] To reduce the computational cost, the Coulomb operator for the HFX calculation was truncated at a radius of 8.0 a_0 and the threshold for the $\varepsilon_{\text{Schwartz}}$ screening parameter was set to 10^{-6}, with screening of the initial density matrix enabled.[64] Level of theory benchmarks on the structural and electronic properties of the complexes and on the oxygen-oxygen radial distribution function are provided in the Appendix, section 4A.7. These tests demonstrate that the level of theory employed is sufficiently accurate for the system of interest in this work.

4.4 Results and discussion

In this work, the $[Ru^{II}(bda)(pic)_2(H_2O)]^+$ (bda = 2,2'-bipyridine-6,6'-dicarboxylic acid, pic = 4-picoline) complex was considered as the water oxidation catalyst. This catalyst has been reported to operate with a catalytic turnover frequency (TOF) of 32 s^{-1} and is representative of a class of ruthenium-based catalysts developed in the groups of Sun and Llobet.[9] Although other catalysts have been reported to perform at higher turnover frequencies, these catalysts typically rely on different axial ligands which increase π- π stacking interactions, leading to higher intermolecular collision frequencies that favor the I2M pathway.[15,19] Since the purpose of this work is to study the mononuclear WNA mechanism, it is

reasonable to consider the smaller 4-picoline ligand, as this saves computational resources. We note that the catalyst with 4-picoline axial ligands has been reported to perform very similarly to its phenylpyridine counterpart once it had been immobilized in a supramolecular assembly on a TiO_2 surface (see ref [11], Figure 4.2b). This type of catalyst has been adopted in several studies on catalyst and photosensitizer functionalized photoanodes.[11,20,21,65–74]

The organic 2,6-diethoxy-1,4,5,8-diimidenapthalene (NDI) dye was employed as photon absorber. This dye has been studied extensively and computational work has shown that it has the appropriate redox properties to provide a driving force for all four PCET steps in the water oxidation process in similar catalysts.[75–77] The NDI molecule was covalently bound to the catalyst on the nitrogen position of one of the imide moieties (see Figure 4.1). Computational work in our group has shown that photo-induced electron injection from the NDI to the TiO_2 surface is fast compared to the kinetics of the catalyst,[78,79] which is consistent with experimental works on other dye-TiO_2 interfaces.[80–82] The TiO_2 was, therefore, not taken into account explicitly and the photoinduced electron injection was simulated by instantaneous oxidation of the dye molecule. Experimental works, as well as *in silico* efforts, have focused on elucidating the reaction mechanism for the $[Ru^{II}(bda)(pic)_2(H_2O)]^+$ catalyst.[15] Based on these investigations and the research reported in this work, a reaction mechanism is proposed for the catalyst-dye complex. The proposed catalytic cycle is depicted in Figure 4.1. The catalyst is activated by oxidation of the Ru^{II} complex to form a Ru^{III}-OH_2 intermediate. Subsequently, a series of four proton coupled electron transfer steps lead to formation of Ru^{IV}-OH, Ru^{V}=O, Ru^{IV}-OOH and finally again the Ru^{III}-OH_2. It has been found in earlier research that during the entire catalytic cycle the ruthenium remains in the low-spin electronic configuration.[83] In this work, we have simulated with DFT based molecular dynamics all four PCET steps of the catalyst-dye complex. Simulations of the first and second PCET step were found to proceed on a fast timescale and are discussed in the Appendix, sections 4A.3 and 4A.4. The first section in the results concerns the equilibrium dynamics of the

Ru^{III}-bda intermediate before the first PCET step, as the nature of this equilibrium is still under debate in literature. Subsequently, the paper focusses on the rate-limiting third PCET step and the fourth PCET step which is rapidly followed by release of the dioxygen ligand.

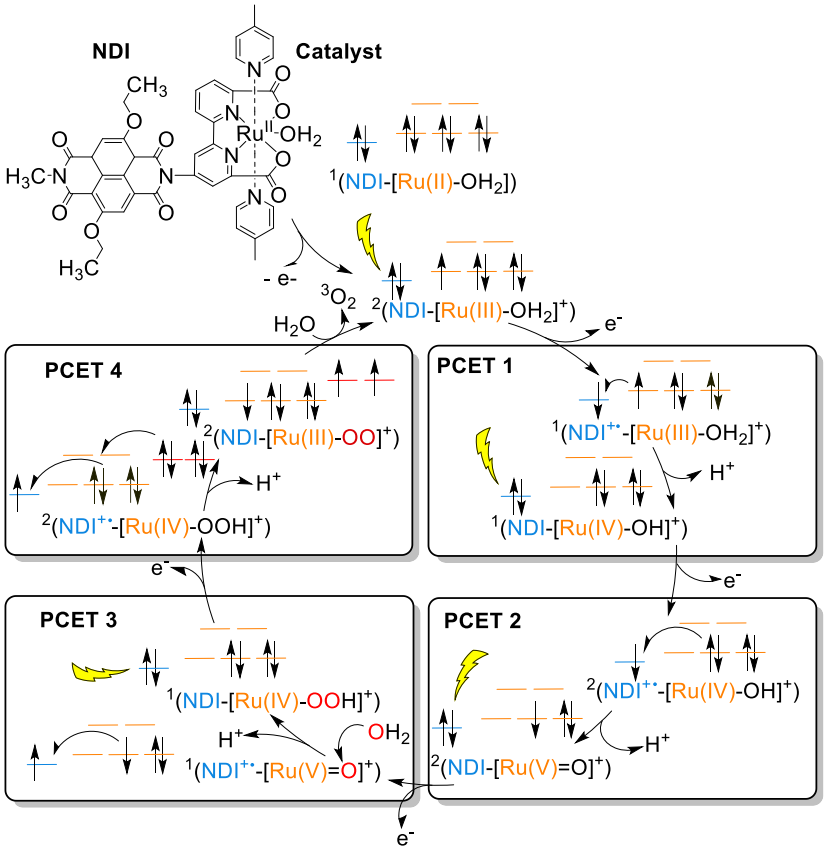

Figure 4.1. *The proposed catalytic cycle for the studied WOC-dye system. Initially, the Ru(II) complex is oxidized to Ru(III). Then, four photo-induced PCET steps lead to formation of one dioxygen molecule, four protons and four electrons. A schematic representation of the electronic configuration on the ruthenium center at each intermediate is depicted in orange and the HOMO energy level of the dye is depicted in blue. The photo-oxidation events are highlighted by the yellow flash symbols. In the third and fourth PCET steps, the high valent ruthenium is reduced with electrons coming from the hydroperoxo/oxygen ligand.*

Those orbitals are depicted in red. Both in PCET step 1 and step 3, the singlet spin-multiplicity is preserved during the reaction, despite the initial open shell character of the system.

4.4.1 Probing the equilibrium dynamics of the low-valent Ru^{III}-bda intermediate

From a combination of X-ray, NMR, and EPR studies, three distinct binding modes have been resolved for Ru^{III}-bda complexes.[16–18] In the first binding mode, one of the carboxylate groups is reported to dissociate from the ruthenium, leading to a k^3-O^1N^2 coordination, whereas in the second binding mode the Ru-$N_{bda^{2-}}$ is elongated, leading to a k^3-O^2N^1 coordination.[17,18] Recently, also a complex has been isolated in which the aqua ligand exhibits a weak interaction with the ruthenium, while the bda^{2-} backbone binds symmetrically in a k^4-O^2N^2 binding mode.[16] In order to gain insights into the dynamic behavior of the catalyst in this low-valent oxidation state, we performed simulations both employing the PBE and the B3LYP exchange-correlation functionals. The ^{2}(NDI-[Ru(III)-OH_2])$^+$ complex was equilibrated at the GGA-PBE level for 3 ps and subsequently propagated for another 5 ps at room temperature. Then the simulation was continued for another 4.6 ps at the hybrid level.

Interestingly, the complex was found to exhibit a dynamic equilibrium in which all binding modes discussed above participate. Snapshots of the trajectory where the system is in the k^4-O^2N^2, k^3-O^1N^2 and k^3-O^2N^1 binding modes are provided in Figure 4.2a, b and c, respectively. These figures also indicate with colors the Ru-O_{H_2O}, Ru-O_{COO^-} and Ru-$N_{bda^{2-}}$ bonds that coordinate and dissociate from the ruthenium center. The time evolution of these bonds during the PBE and B3LYP simulations is visualized in Figure 4.2d. The other Ru-O_{COO^-} and Ru-$N_{bda^{2-}}$ distances, as well as the axial Ru-N_{pic} distances, were found to remain relatively stable during the MD simulation and are provided in the Appendix, Figure 4A.3 and Figure 4A.4. In the performed PBE-based simulations, it was found that the system resides in a dynamic equilibrium between two six-coordinated, pseudo-

octahedral complexes, where the aqua ligand and one of the bda-carboxyl groups rapidly coordinate and dissociate to the Ru^{III} center on the sub-ps timescale. Interestingly, the binding of the aqua ligand was paired with the formation of strong hydrogen bonding interactions between the aqua ligand and the surrounding water molecules. Remarkably, at the B3LYP level of theory the dynamic behavior of the complex was preserved, but now also involving the k^3-O^2N^1 binding mode, where the equatorial Ru-$N_{bda^{2-}}$ distance is elongated, see parts of the trajectory between 5.2-5.4 ps and 9.1-9.5 ps in Figure 4.2. It was also attempted to equilibrate this k^3-O^2N^1 complex at the PBE level by constraining the equatorial Ru-$N_{bda^{2-}}$ distance to 2.54 Å and equilibrating the system for 2.5 ps. However, after lifting the constraint the system was found to relax instantaneously to the k^3-O^1N^2 coordination mode.

It can be concluded that the barriers associated with the transitions between the different binding modes are low. The aqua ligand is found to remain close to the metal center (< 3.0 Å) at all times during the simulation, even in the case of k^4-O^2N^2 coordination of the bda^{2-} ligand. This pseudo-7-coordinated environment implies that the first step in the catalytic cycle is not limited by slow coordination of the aqua ligand to the Ru(III) center. These results underscore how DFT-MD with explicit solvent can help to understand the dynamical flexibility in the coordination sphere of transition metal complexes.

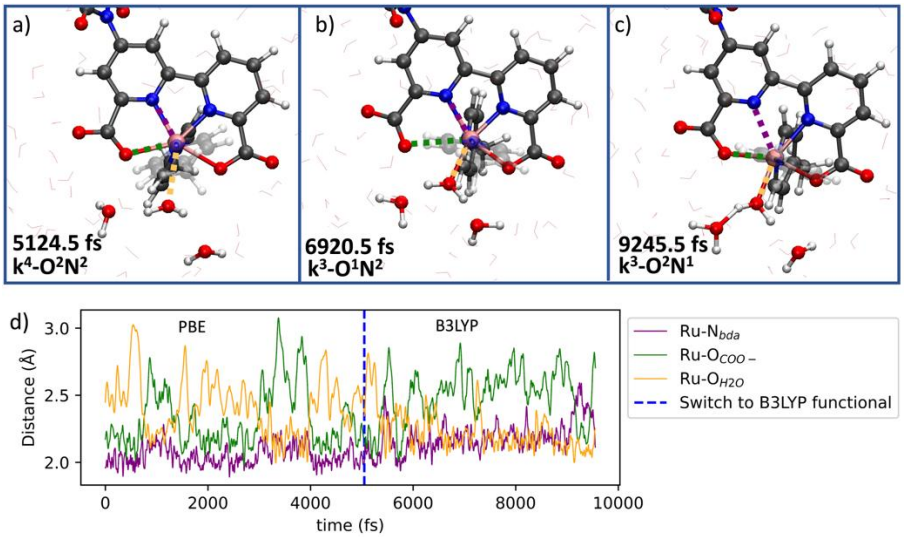

Figure 4.2. *Snapshots from the AIMD simulations that represent the three binding modes, k^4-O^2N^2 (a), k^3-O^1N^2 (b) and k^3-O^2N^1 (c), are displayed in the top panel. The time evolution of Ru-$N_{bda}{}^{2-}$, Ru-$O_{COO}{}^-$ and Ru-O_{H_2O} bonds are plotted in d). In panel d), the first half of the trajectory is propagated at the GGA-PBE level, while the second half of the trajectory is propagated at the hybrid-B3LYP level of theory.*

4.4.2 Blue Moon simulations of the rate-determining O-O bond formation step

The first and second photo-induced proton-coupled electron transfer (PCET) steps in the catalytic cycle of the investigated catalyst-dye dyad were found to proceed fast, on the ab initio MD time scale of several picoseconds (see Appendix, section 4A.3 and 4A.4). Consequently, we shift our attention to the third PCET event (PCET 3 in Figure 4.1). We employed a similar strategy as in the previous section: the equilibration of the system and exploratory Metadynamics (MetaD) and Blue Moon ensemble simulations were performed at the GGA-PBE level of theory, followed by an additional ~1 ps propagation of the Blue Moon ensemble trajectories at the hybrid-B3LYP level to refine the results. This approach enables us to compare the obtained free energy surface (FES) at both levels of theory. This section describes in more detail the performed enhanced sampling simulations.

The high-valent ^{2}(NDI-[Ru(V)=O])$^{+}$ complex was equilibrated at room temperature for ~4 ps at the GGA-PBE level of theory. During this simulation, the spin density was localized exclusively on the ruthenium t_{2g} and the oxygen p orbitals (see Appendix, section 4A.5, Figure 4A.8). Despite the considerable electron deficient character of the oxygen, essentially no nucleophilic coordination of water molecules was observed in the performed simulations. This is in accordance with other *in silico* studies that reported the Ru=O moiety to be hydrophobic.[19] The Ru-O distance was found to fluctuate around 1.72 ±0.05 Å, which is in excellent agreement with in-situ X-ray absorption spectroscopy studies on this catalyst class, that report a value of 1.75 ±0.02 Å. [84] At this stage, the complex was found strictly in the 7-coordinated environment with a symmetric binding of the carboxyl groups, although both Ru-O bonds fluctuated appreciably. After the removal of one alpha-spin electron from the dye, the system was found to equilibrate to a stable open-shell singlet with one unpaired alpha-electron on the catalyst and one unpaired beta-electron on the dye (see Figure 4A.9). This complex was found to remain stable over the course of 3 ps, without attempting electron transfer or interaction with nearby water molecules.

In order to observe the slow O-O bond formation, the water nucleophilic attack was accelerated by employing the well-tempered MetaD enhanced sampling method, of which the details are discussed in the appendix, 4A.6.1.[85] The O-O distance between the oxo ligand and the nearest water molecule in the solvent was chosen as collective variable (CV), similar to previous studies.[26,29,75] We argue that this choice of the CV is justified, given that one cannot discriminate between different water molecules in the simulation and the system is sufficiently equilibrated before we start the MetaD. Notably, the carboxylate group of the bda^{2-} ligand acted as a hydrogen bond acceptor towards one of the protons of the nucleophilic water molecule during the final ~22 ps of the MetaD simulation, even though this interaction was not included in the collective variable along which the reaction was biased (see Figure 4.3). Nevertheless, the PCET event consistently

involved dissociation of the proton facing the water environment, and not the one involved in this interaction. Although the MetaD simulations yielded a reactive trajectory, the statistical error in the obtained free energy surface (FES) remained large within the timescale that we could afford to run the simulation (see Appendix, Figure 4A.10).

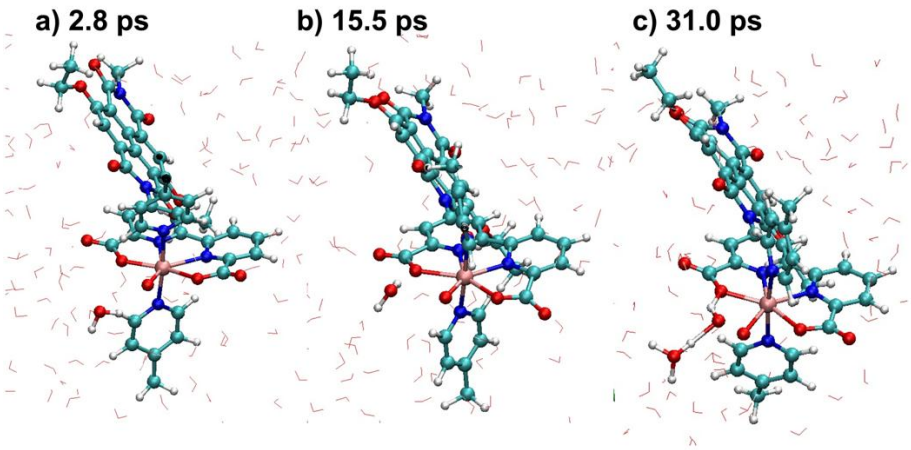

Figure 4.3. *Three stages during the third PCET reaction, forming the O-O bond. (a) The water molecule roams around freely. (b) One of the protons on the water molecule forms a hydrogen bond with the carboxylate group of the* bda^{2-} *ligand. (c) The O-O bond is formed, while simultaneously the water facing proton is abstracted following a Grotthüs mechanism.*

The FES was further refined following the Blue Moon approach using the O-O distance as collective variable.[86,87] Nine structures were sampled from the MetaD simulation with O-O distances between 3.0 and 1.4 Å at 0.2 Å intervals. These structures were subsequently used as input for GGA-PBE based MD simulations, in which their O-O distance was constrained. After the averaged constraint force λ for each MD simulation had converged to a stable value, the trajectories were propagated for another $1.5<t<3$ ps, after which a constraint force profile was constructed from the averaged λ values (see Appendix, Figure 4A.11 a). Two

additional points were added to this profile at 1.45 Å and 3.3 Å. Unconstrained DFT-MD simulations showed that these values present the equilibrium O-O distances in the reactant and product states of the complex (see Appendix, section 4A.6.2). The profile was fitted with a 100-point Akima spline, and subsequently numerically integrated to obtain the FES (see Appendix, Figure 4A.11 b). The equilibrated GGA-PBE trajectories were further propagated for another ~1 ps at the hybrid-B3LYP level, after which this procedure was repeated to generate the force profile and FES at the hybrid-DFT level (Figure 4.4a and b). To improve the resolution in the region of the transition state, two additional points, at 2.1 and 1.9 Å, were considered at the hybrid-level. Errors on the λ-profile and FES were obtained from block averaging. Details on this procedure and further details on the Blue Moon approach are provided in the Appendix, 4A.6.2.

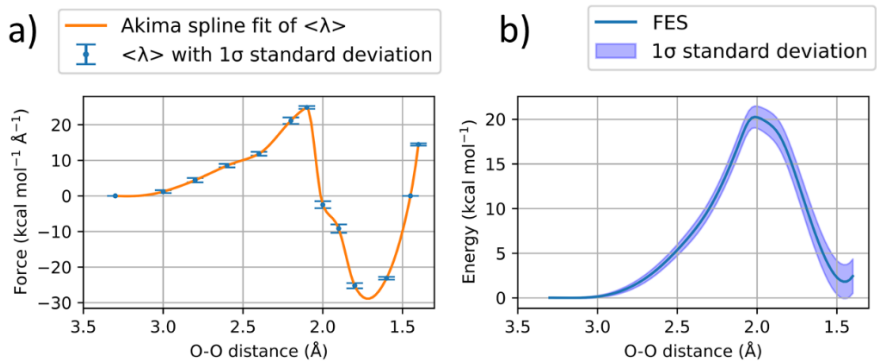

Figure 4.4. *FES calculated at the B3LYP level, plotted as a function of the O-O distance reaction coordinate. The free energy was obtained by thermodynamic integration of a 100-point Akima spline fit of the averaged constraint forces, <λ>, at different values of the constrained O-O bond distance. The error bars on <λ> are obtained by block averaging. The error on the FES is calculated by integrating the upper and lower bounds of the <λ> profile.*

The hybrid-B3LYP based Blue Moon ensemble simulations predict a 20.3 ± 1.2 kcal mol^{-1} free energy barrier governing the O-O bond formation. The overall

reaction has a free energy difference of 1.8 ± 1.9 kcal mol^{-1}, indicating that, within the statistical error, the reaction is endothermic with the selected NDI dye. Previous studies from our group on different catalysts with the same dye showed a larger driving force for the O-O bond formation, likely because those catalysts involved Ru in a lower oxidation state.[75,76] Experimentally, the half wave potential $E_{1/2}$ for the employed NDI dye has been measured at 1.36 V vs Fc/Fc^{+},[88] which thus appears to be the minimum required oxidation potential for mononuclear water oxidation catalysis with this Ru-bda catalyst.[77] While the relatively low barrier suggests the viability of the WNA mechanism as a potential route, the associated rate constant of ~0.008 s^{-1} (min = 0.001 s^{-1}, max= 0.06 s^{-1}) is four to eight orders of magnitude slower than the rates achieved through the I2M mechanism with this catalyst.[15] We have also calculated the reaction profile at the GGA-PBE level (see the Appendix, Figure 4A.11). Interestingly, the overall reaction is found to be endothermic at that level with a ΔG = 2.9 ± 0.9 kcal mol^{-1}. The barrier at the GGA-level is lower than at the hybrid-level, with the $\Delta G^{\ddagger}$ = 14.9 ± 0.9 kcal mol^{-1}. Note that the error bar at the GGA-level is smaller than at the hybrid-B3LYP level since the GGA is computationally more efficient and simulations can be run over a longer timescale.

To get an understanding of the observed differences between the two functional set-ups, we have evaluated the proton and electron transfer dynamics during the Blue Moon ensemble simulations. In these simulations, the proton involved in the PCET reaction was not constrained and, therefore, free to dissociate from the nucleophilic water molecule. In addition, the electron could move freely from the catalyst to the photo-oxidized dye. In Figure 4.5, panel a, the spin density of the initial state corresponding to an open-shell singlet spin configuration with an unpaired electron on the catalyst and a hole on the dye is shown (see also Figure 4.1, PCET 3). After the third PCET step, a singlet closed shell configuration is obtained, where the unpaired electron on the catalyst has recombined with the hole (Figure 4.5, panel b). In Figure 4.5, panels c and d, the hybrid-B3LYP and GGA-PBE spin density evolution is visualized for the duration of 400 fs during the Blue

Moon simulations with constrained O-O distances of 3.0 Å, 2.2 Å, 2.0 Å and 1.4 Å. Figure 4.5c displays the first 400 fs for the hybrid simulations, while Figure 4.5d provides the 400 fs in which the PCET event takes places in the 2.0 Å GGA-based simulation.

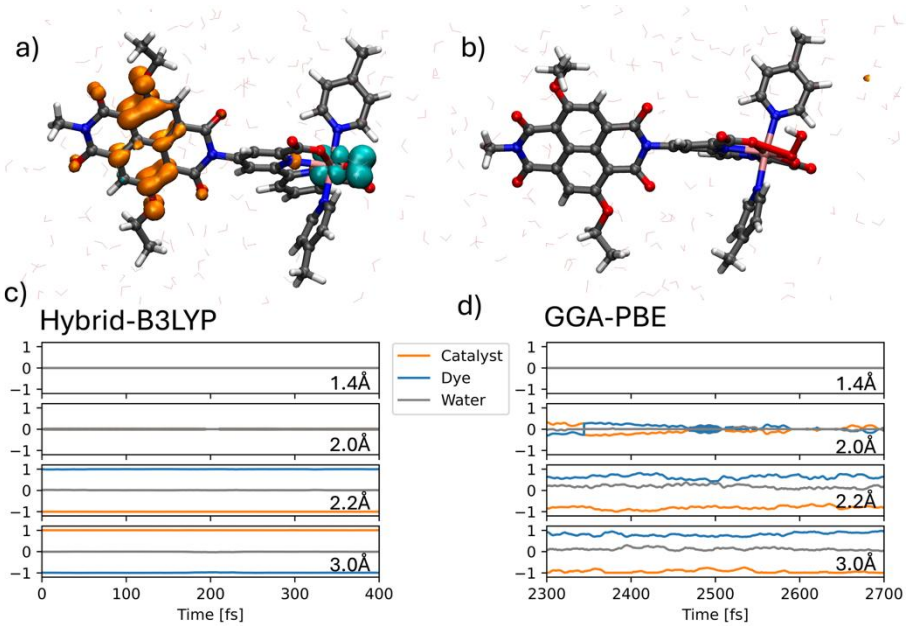

Figure 4.5. *The top panels provide a visualization of the spin density of snapshots taken from the hybrid-B3LYP simulations with constrained O-O distances of 3.0 Å (a) and 1.4 Å (b), where the isosurface values were set to 0.003 for positive, and -0.003 for negative spin density contributions. Panels c) and d) plot the spin density population analysis on the catalyst (orange), dye (blue) and water (grey) as a function of simulation time. The local spin density on the specified fragments was obtained by summing over the atomic Mulliken spin density contributions.*

Figure 4.5 shows that the simulations with constrained O-O distances longer than 2.0 Å exhibit consistently an open shell singlet spin-multiplicity, where the hole is located on the dye. The application of the pure-DFT functional leads to a

considerable fraction of spin density on the water solvent molecules. This is a commonly known artifact of GGA-based DFT.[33,34] Interestingly, this spin delocalization is virtually eliminated in the simulations with the hybrid-B3LYP functional. The tendency of B3LYP to localize the spin density better than PBE becomes particularly apparent when the O-O distance is shortened to 2.2 Å. At that point, the integrated spin density on the dye is reduced to ~0.6 at the GGA level, indicating that the electron and hole are formed only partially. In contrast, the spin localization on the dye is preserved at the hybrid-B3LYP level. The GGA simulation at 2.0 Å shows that the electron-hole pair separation collapses after 2500 fs, which was found to coincide with the proton transfer event. In the simulations with an O-O bond distance shorter than 2.0 Å, the system forms consistently a closed-shell singlet, where the electron has transferred to the dye.

4.4.3 Dioxygen dissociation after the fourth PCET step

The initial structure for the equilibration simulations of the ^{1}([Ru(IV)-OOH]-NDI)$^{+}$ intermediate was extracted from the final part of the trajectory of the third PCET step, where the excess proton was removed from the water solvation environment. The system was equilibrated at the PBE level at room temperature for 2 ps before once more the photooxidation of the NDI was simulated by removing an electron from the simulation box. The evolution of the spin density on the dye, catalyst, and the water environment are plotted over time in Figure 4.6a in the top panel, while the dissociating O-H distance from the hydroperoxo ligand is shown in the bottom panel.

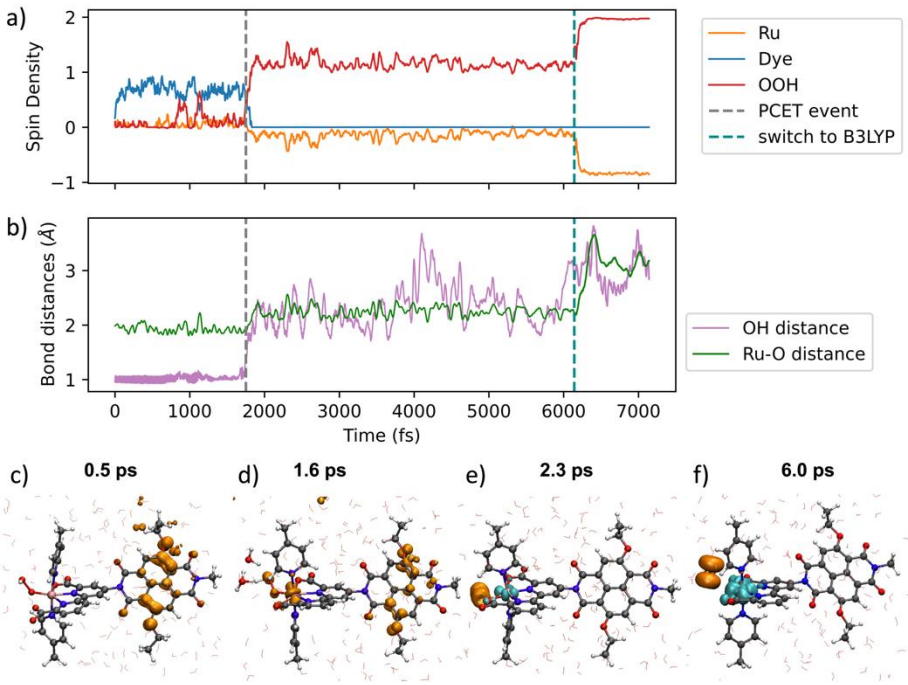

Figure 4.6. *a) The red, blue, and orange traces represent the integrated spin moments on the O-O ligand, NDI dye, and ruthenium center, respectively. b) The purple line represents the length of the dissociating O-H bond, while the green line represents the Ru-O distance. c), d), e), and f) provide visualizations of the spin density at four stages which are characteristic for the PCET reaction. Isosurface values were set to 0.003 for positive, and -0.003 for negative spin density contributions.*

Although the hole is initially delocalized over the solvent water molecules, most of the spin density localizes on the NDI within the first ~100 fs after oxidation of the system (Figure 4.6a and c). In the following ~1.7 ps the system remains in a stable state with the proton attached to the O-O ligand. Interestingly, two attempted electron transfers are observed prior to the final PCET event, at around 0.9 ps and 1.1 ps. At this stage, a water molecule is closely coordinated to the hydroperoxo ligand, however, there is no chain of water molecules to facilitate

long-range proton transfer. Subsequently, a second water molecule was observed to form a hydrogen bond interaction with the water molecule coordinating to the hydroperoxo ligand, allowing for the PCET event to occur (see Figure 4.6d). After the PCET, significant oscillations are observed of the spin density moving between the metal center and the oxygen ligand. Nevertheless, the performed simulations employing the PBE functional eventually appeared to favor a configuration where one of the triplet oxygen electrons recombines with the anti-ferromagnetically coupled ruthenium electron, forming what is best described as a doublet spin configuration on the oxygen ligand (see Figure 4.6e). This species remained stable over more than 4 ps of simulation time. Since GGA functionals are known to overestimate charge delocalization, it was decided to propagate the system for another 1 ps with the B3LYP functional.[32–34] By including a fraction of screened-Hartree-Fock exchange, the two unpaired electrons localized on the dioxygen ligand exclusively, forming a local triplet (see Figure 4.6f). Consequently, the O_2 ligand dissociated rapidly from the catalyst after switching to the hybrid functional. This observation underlines the importance of including a fraction of exact exchange in this type of simulations and should be kept in mind for future studies on similar systems.

4.5 Conclusions

In summary, DFT-based molecular dynamics simulations were performed of the four proton-coupled electron transfer (PCET) steps in the catalytic water oxidation cycle of a $[Ru^{III}(bda)(pic)_2(H_2O)]^+$ (bda = 2,2'-bipyridine-6,6'-dicarboxylic acid, pic = 4-picoline) catalyst, covalently bound to the 2,6-diethoxy-1,4,5,8-diimidenapthalene (NDI) dye. The first part of this work addresses the coordination environment of the ruthenium center at the beginning of the catalytic cycle. The dynamics simulations reveal that the low valent $[Ru^{III}(bda)(pic)_2(H_2O)]^+$ intermediate adopts a six-coordinated configuration, wherein coordination of the aqua ligand is followed by a lowering of the coordination number of the bda^{2-} ligand, either by elongation of the equatorial Ru-

$N_{bda^{2-}}$ bond or by elongation of the equatorial Ru-O_{COO^-} bond. Following the first PCET step, the resulting $[Ru^{IV}(bda)(pic)_2(OH)]^+$ complex consistently maintained a 7-coordinated environment. This 7-coordinated environment is preserved also after the second, third, and fourth PCET steps.

To gain an understanding of the behavior of this catalyst when anchored to a surface, the O-O bond-forming step was considered to involve the nucleophilic attack of a water molecule on a single, high valent Ru^V=O species. Using Blue Moon ensemble simulations at the B3LYP level, the barrier for this process was determined to be 20.3±1.2 kcal mol^{-1}, corresponding to a catalytic rate of approximately 0.008 s^{-1} (min = 0.001 s^{-1}, max= 0.06 s^{-1}) at 300 K. This rate represents a realistic estimate for systems where the catalyst is immobilized, and is four to eight orders of magnitude slower than the rates that have been reported in studies where the catalyst followed the binuclear mechanism.[9,15] The oxidation potential of the employed NDI dye, which has been measured at 1.36 V vs Fc/Fc^+,[88] was found to be slightly insufficient to drive the O-O bond formation. We found that the subsequent and final PCET step, in which the hydroperoxo ligand is oxidized to form O_2, happened spontaneously on the ab initio molecular dynamics timescale and will, therefore, not affect much the kinetics of the catalyst.

Finally, we have evaluated the performance of the widely used GGA-PBE and the hybrid-B3LYP functionals in determining the reaction barriers, energetics, and description of spin localizations in the DFT-based molecular dynamics simulations. In addition to the slight changes in the relative energies of reactant and product states for the rate-determining O-O bond formation, it was found that the GGA functional exhibits a tendency to overestimate delocalization of spin density, leading to significant spin polarizations on the water environment and unphysical pairing of electrons on the O_2 ligand with an electron on the ruthenium center. The inclusion of exact exchange quenches delocalization, leading to the electron and hole densities that are localized on the catalyst and dye fragments of the system. The most notable effect of this correction on the dynamics was

observed for the dissociation of the O_2 ligand at the end of the catalytic cycle, which happened spontaneously with the hybrid functional while in the simulations with the GGA functional the oxygen molecule remained bound to the ruthenium complex.

4.6 References

[1] S. Ardo, D. Fernandez Rivas, M. A. Modestino, V. Schulze Greiving, F. F. Abdi, E. Alarcon Llado, V. Artero, K. Ayers, C. Battaglia, J. P. Becker, D. Bederak, A. Berger, F. Buda, E. Chinello, B. Dam, V. Di Palma, T. Edvinsson, K. Fujii, H. Gardeniers, H. Geerlings, S. M. Hashemi, S. Haussener, F. Houle, J. Huskens, B. D. James, K. Konrad, A. Kudo, P. P. Kunturu, D. Lohse, B. Mei, E. L. Miller, G. F. Moore, J. Muller, K. L. Orchard, T. E. Rosser, F. H. Saadi, J. W. Schüttauf, B. Seger, S. W. Sheehan, W. A. Smith, J. Spurgeon, M. H. Tang, R. Van De Krol, P. C. K. Vesborg, P. Westerik, *Energy Environ. Sci.* **2018**, *11*, 2768–2783.

[2] H. Tian, *Sustain. Energy Fuels.* **2019**, *3*, 888–898.

[3] J. H. Kim, D. Hansora, P. Sharma, J.-W. Jang, J. S. Lee, *Chem. Soc. Rev.* **2019**, *48*, 1908–1971.

[4] S. Haussener, *Sol. Energy* **2022**, *246*, 294–300.

[5] M. Grätzel, *Nature.* **2001**, *414*, 338–344.

[6] A. Vilanova, P. Dias, T. Lopes, A. Mendes, *Chem. Soc. Rev.* **2024**, *53*, 2388–2434.

[7] S. Nitopi, E. Bertheussen, S. B. Scott, X. Liu, A. K. Engstfeld, S. Horch, B. Seger, I. E. L. Stephens, K. Chan, C. Hahn, J. K. Nørskov, T. F. Jaramillo, I. Chorkendorff, *Chem. Rev.* **2019**, *119*, 7610–7672.

[8] J. Seo, H. Nishiyama, T. Yamada, K. Domen, *Angew. Chem. Int. Ed.* **2018**, *57*, 8396–8415.

[9] L. Duan, F. Bozoglian, S. Mandal, B. Stewart, T. Privalov, A. Llobet, L. Sun, *Nat. Chem.* **2012**, *4*, 418–423.

[10] J. Yang, L. Wang, S. Zhan, H. Zou, H. Chen, M. S. G. Ahlquist, L. Duan, L. Sun, *Nat. Commun.* **2021**, *12*, 373.

[11] H. Li, F. Li, Y. Wang, L. Bai, F. Yu, L. Sun, *ChemPlusChem* **2016**, *81*, 1056–1059.

[12] D. L. Ashford, W. Song, J. J. Concepcion, C. R. K. Glasson, M. K. Brennaman, M. R. Norris, Z. Fang, J. L. Templeton, T. J. Meyer, *J. Am. Chem. Soc.* **2012**, *134*, 19189–19198.

[13] L. Alibabaei, M. K. Brennaman, M. R. Norris, B. Kalanyan, W. Song, M. D. Losego, J. J. Concepcion, R. A. Binstead, G. N. Parsons, T. J. Meyer, *Proc. Natl. Acad. Sci. U.S.A.* **2013**, *110*, 20008–20013.

[14] J. T. Kirner, J. J. Stracke, B. A. Gregg, R. G. Finke, *ACS Appl. Mater. Interfaces* **2014**, *6*, 13367–13377.

[15] B. Zhang, L. Sun, *J. Am. Chem. Soc.* **2019**, *141*, 5565–5580.

[16] T. Liu, G. Li, N. Shen, L. Wang, B. J. J. Timmer, S. Zhou, B. Zhang, A. Kravchenko, B. Xu, M. S. G. Ahlquist, L. Sun, *CCS Chem.* **2022**, *4*, 2481–2490.

[17] R. Matheu, A. Ghaderian, L. Francàs, P. Chernev, M. Z. Ertem, J. Benet-Buchholz, V. S. Batista, M. Haumann, C. Gimbert-Suriñach, X. Sala, A. Llobet, *Chem. Eur. J.* **2018**, *24*, 12838–12847.

[18] Q. Daniel, P. Huang, T. Fan, Y. Wang, L. Duan, L. Wang, F. Li, Z. Rinkevicius, F. Mamedov, M. S. G. Ahlquist, S. Styring, L. Sun, *Coord. Chem. Rev.* **2017**, *346*, 206–215.

[19] S. Zhan, D. Mårtensson, M. Purg, S. C. L. Kamerlin, M. S. G. Ahlquist, *Angew. Chem. Int. Ed.* **2017**, *56*, 6962–6965.

[20] D. Wang, S. L. Marquard, L. Troian-Gautier, M. V. Sheridan, B. D. Sherman, Y. Wang, M. S. Eberhart, B. H. Farnum, C. J. Dares, T. J. Meyer, *J. Am. Chem. Soc.* **2018**, *140*, 719–726.

[21] D. Wang, M. S. Eberhart, M. V. Sheridan, K. Hu, B. D. Sherman, A. Nayak, Y. Wang, S. L. Marquard, C. J. Dares, T. J. Meyer, *Proc. Natl. Acad. Sci. U.S.A.* **2018**, *115*, 8523–8528.
[22] X. Yan, K. Sakai, H. Ozawa, *ACS Catal.* **2023**, *13*, 13456–13465.
[23] H. Song, A. Amati, A. Pannwitz, S. Bonnet, L. Hammarström, *J. Am. Chem. Soc.* **2022**, *144*, 19353–19364.
[24] J. Feng, X. Li, Y. Luo, Z. Su, M. Zhong, B. Yu, J. Shi, *Chinese J. Catal.* **2023**, *48*, 127–136.
[25] D. W. Shaffer, Y. Xie, J. J. Concepcion, *Chem. Soc. Rev.* **2017**, *46*, 6170–6193.
[26] N. Govindarajan, A. Tiwari, B. Ensing, E. J. Meijer, *Inorg. Chem.* **2018**, *57*, 13063–13066.
[27] M. Schilling, R. A. Cunha, S. Luber, *J. Chem. Theory Comput.* **2020**, *16*, 2436–2449.
[28] M. Schilling, R. Ketkaew, S. Luber, *Chimia* **2021**, *75*, 195–201.
[29] M. Schilling, R. A. Cunha, S. Luber, *ACS Catal.* **2020**, *10*, 7657–7667.
[30] K. R. Gorantla, B. S. Mallik, *J. Phys. Chem. C* **2020**, *124*, 205–218.
[31] K. R. Gorantla, B. S. Mallik, *J. Phys. Chem. A* **2022**, *126*, 3301–3310.
[32] Aron J. Cohen, Paula Mori-Sánches, Weitao Yang, *Science* **2008**, *321*, 792–794.
[33] C. Li, X. Zheng, N. Q. Su, W. Yang, *Natl. Sci. Rev.* **2018**, *5*, 203–215.
[34] K. R. Bryenton, A. A. Adeleke, S. G. Dale, E. R. Johnson, *WIREs Comput. Mol. Sci.* **2023**, *13*, e1631.
[35] J. Cheng, M. Sulpizi, J. VandeVondele, M. Sprik, *ChemCatChem* **2012**, *4*, 636–640.
[36] M. Guidon, J. Hutter, J. VandeVondele, *J. Chem. Theory Comput.* **2010**, *6*, 2348–2364.
[37] T. de Haas, H. van Overeem, H. J. M. de Groot, F. Buda, *ChemPhotoChem* **2022**, e202200274.
[38] L. Martínez, R. Andrade, E. G. Birgin, J. M. Martínez, *J. Comput. Chem.* **2009**, *30*, 2157–2164.
[39] AMS2022.102, SCM, Theoretical Chemistry. Vrije Universiteit: Amsterdam, The Netherlands. https://www.scm.com.
[40] D. Van Der Spoel, E. Lindahl, B. Hess, G. Groenhof, A. E. Mark, H. J. C. Berendsen, *J. Comput. Chem.* **2005**, *26*, 1701–1718.
[41] W. L. Jorgensen, J. Chandrasekhar, J. D. Madura, R. W. Impey, M. L. Klein, *J. Chem. Phys.* **1983**, *79*, 926–935.
[42] W. L. Jorgensen, D. S. Maxwell, J. Tirado-Rives, *J. Am. Chem. Soc.* **1996**, *118*, 11225–11236.
[43] L. S. Dodda, I. Cabeza de Vaca, J. Tirado-Rives, W. L. Jorgensen, *Nucleic Acids Res.* **2017**, *45*, W331–W336.
[44] W. L. Jorgensen, J. Tirado-Rives, *Proc. Natl. Acad. Sci. U.S.A.* **2005**, *102*, 6665–6670.
[45] L. S. Dodda, J. Z. Vilseck, J. Tirado-Rives, W. L. Jorgensen, *J. Phys. Chem. B* **2017**, *121*, 3864–3870.
[46] C. E. S. Bernardes, José. N. Canongia Lopes, M. E. M. Da Piedade, *J. Phys. Chem. A* **2013**, *117*, 11107–11113.
[47] H. J. C. Berendsen, J. P. M. Postma, W. F. Van Gunsteren, A. DiNola, J. R. Haak, *J. Chem. Phys.* **1984**, *81*, 3684–3690.
[48] M. Parrinello, A. Rahman, *J. Appl. Phys.* **1981**, *52*, 7182–7190.
[49] S. Nosé, M. L. Klein, *Mol. Phys.* **1983**, *50*, 1055–1076.
[50] T. D. Kühne, M. Iannuzzi, M. Del Ben, V. V. Rybkin, P. Seewald, F. Stein, T. Laino, R. Z. Khaliullin, O. Schütt, F. Schiffmann, D. Golze, J. Wilhelm, S. Chulkov, M. H. Bani-Hashemian, V. Weber, U. Borštnik, M. Taillefumier, A. S. Jakobovits, A. Lazzaro, H. Pabst, T. Müller, R. Schade, M. Guidon, S. Andermatt, N. Holmberg, G. K. Schenter, A. Hehn, A. Bussy, F. Belleflamme, G. Tabacchi, A. Glöß, M. Lass, I. Bethune, C. J. Mundy, C. Plessl, M. Watkins, J. VandeVondele, M. Krack, J. Hutter, *J. Chem. Phys.* **2020**, *152*, 194103.
[51] J. P. Perdew, K. Burke, M. Ernzerhof, *Phys. Rev. Lett.* **1997**, *78*, 1396–1396.
[52] S. Grimme, *J. Comput. Chem.* **2004**, *25*, 1463–1473.
[53] S. Grimme, *Wiley Interdiscip. Rev. Comput. Mol. Sci.* **2011**, *1*, 211–228.

[54] S. Grimme, *Chem. - Eur. J.* **2012**, *18*, 9955–9964.
[55] J. VandeVondele, J. Hutter, *J. Chem. Phys.* **2007**, *127*, 114105
[56] S. Goedecker, M. Teter, J. Hutter, *Phys. Rev. B* **1996**, *54*, 1703–1710.
[57] C. Hartwigsen, S. Goedecker, J. Hutter, *Phys. Rev. B* **1998**, *58*, 3641–3662.
[58] M. Krack, *Theor. Chem. Acc.* **2005**, *114*, 145–152.
[59] J. VandeVondele, J. Hutter, *J. Chem. Phys.* **2003**, *118*, 4365–4369.
[60] A. D. Becke, *Phys. Rev. A.* **1988**, *38*, 3098.
[61] A. D. Becke, *J. Chem. Phys.* **1993**, *98*, 1372–1377.
[62] S. H. Vosko, L. Wilk, M. Nusair, *Can. J. Phys.* **1980**, *58*, 1200–1211.
[63] P. J. Stephen, F. J. Devlin, C. F. Chabalowski, M. J. Frisch, *J. Phys. Chem.* **1994**, *98*, 11623–11627.
[64] M. Guidon, F. Schiffmann, J. Hutter, J. VandeVondele, *J. Chem. Phys.* **2008**, *128*, 214104.
[65] L. Li, L. Duan, Y. Xu, M. Gorlov, A. Hagfeldt, L. Sun, *Chem. Commun.* **2010**, *46*, 7307.
[66] Y. Gao, X. Ding, J. Liu, L. Wang, Z. Lu, L. Li, L. Sun, *J. Am. Chem. Soc.* **2013**, *135*, 4219–4222.
[67] H. Li, F. Li, B. Zhang, X. Zhou, F. Yu, L. Sun, *J. Am. Chem. Soc.* **2015**, *137*, 4332–4335.
[68] F. Li, K. Fan, L. Wang, Q. Daniel, L. Duan, L. Sun, *ACS Catal.* **2015**, *5*, 3786–3790.
[69] Y. Gao, L. Zhang, X. Ding, L. Sun, *Phys. Chem. Chem. Phys.* **2014**, *16*, 12008.
[70] B. D. Sherman, Y. Xie, M. V. Sheridan, D. Wang, D. W. Shaffer, T. J. Meyer, J. J. Concepcion, *ACS Energy Lett.* **2017**, *2*, 124–128.
[71] M. S. Eberhart, D. Wang, R. N. Sampaio, S. L. Marquard, B. Shan, M. K. Brennaman, G. J. Meyer, C. Dares, T. J. Meyer, *J. Am. Chem. Soc.* **2017**, *139*, 16248–16255.
[72] L. Zhang, Y. Gao, X. Ding, Z. Yu, L. Sun, *ChemSusChem* **2014**, *7*, 2801–2804.
[73] D. Wang, M. V. Sheridan, B. Shan, B. H. Farnum, S. L. Marquard, B. D. Sherman, M. S. Eberhart, A. Nayak, C. J. Dares, A. K. Das, R. M. Bullock, T. J. Meyer, *J. Am. Chem. Soc.* **2017**, *139*, 14518–14525.
[74] M. Yamamoto, Y. Nishizawa, P. Chábera, F. Li, T. Pascher, V. Sundström, L. Sun, H. Imahori, *Chem. Commun.* **2016**, *52*, 13702–13705.
[75] Y. Shao, J. M. De Ruiter, H. J. M. De Groot, F. Buda, *J. Phys. Chem. C.* **2019**, *123*, 21403–21414.
[76] Y. Shao, H. J. M. D. Groot, F. Buda, *ChemSusChem.* **2020**, *13*, 1–9.
[77] J. Belić, A. Förster, J. P. Menzel, F. Buda, L. Visscher, *Phys. Chem. Chem. Phys.* **2022**, *24*, 197–210.
[78] J. P. Menzel, A. Papadopoulos, J. Belić, H. J. M. de Groot, L. Visscher, F. Buda, *J. Phys. Chem. C* **2020**, *124*, 27965–27976.
[79] A. Monti, C. F. A. Negre, V. S. Batista, L. G. C. Rego, H. J. M. De Groot, F. Buda, *J. Phys. Chem. Lett.* **2015**, *6*, 2393–2398.
[80] M. Hilgendorff, V. Sundström, *J. Phys. Chem. B* **1998**, *102*, 10505–10514.
[81] R. J. Ellingson, J. B. Asbury, S. Ferrere, H. N. Ghosh, J. R. Sprague, T. Lian, A. J. Nozik, *J. Phys. Chem. B* **1998**, *102*, 6455–6458.
[82] J. B. Asbury, N. A. Anderson, E. Hao, X. Ai, T. Lian, *J. Phys. Chem. B* **2003**, *107*, 7376–7386.
[83] J. P. Menzel, M. Kloppenburg, J. Belić, H. J. M. de Groot, L. Visscher, F. Buda, *J. Comput. Chem.* **2021**, *42*, 1885–1894.
[84] D. Lebedev, Y. Pineda-Galvan, Y. Tokimaru, A. Fedorov, N. Kaeffer, C. Copéret, Y. Pushkar, *J. Am. Chem. Soc.* **2018**, *140*, 451–458.
[85] A. Barducci, G. Bussi, M. Parrinello, *Phys. Rev. Lett.* **2008**, *100*, 020603.
[86] M. Sprik, G. Ciccotti, *J. Chem. Phys.* **1998**, *109*, 7737–7744.
[87] G. Ciccotti, M. Ferrario, *Mol. Sim.* **2004**, *30*, 787–793.
[88] R. S. K. Kishore, O. Kel, N. Banerji, D. Emery, G. Bollot, J. Mareda, A. Gomez-Casado, P. Jonkheijm, J. Huskens, P. Maroni, M. Borkovec, E. Vauthey, N. Sakai, S. Matile, *J. Am. Chem. Soc.* **2009**, *131*, 11106–11116.

4A. Appendix

4A.1 Calculation of the reaction rates from the activation free energies

The reaction rates reported in this paper were calculated according to the following equation from transition state theory:[1,2]

$$k = \frac{k_B T}{h} e^{\frac{-\Delta G}{RT}}$$

Where k is the reaction rate, k_B is the Boltzmann constant, T is the temperature, h is Planck's constant, ΔG is the activation energy and R is the universal gas constant.

4A.2 Equilibrations of the ^{2}(NDI-[Ru(III)-OH$_2$]$^+$), ^{1}(NDI-[Ru(IV)-OH]$^+$), ^{2}(NDI-[Ru(V)=O]$^+$), and ^{1}(NDI-[Ru(IV)-OOH]$^+$) intermediates

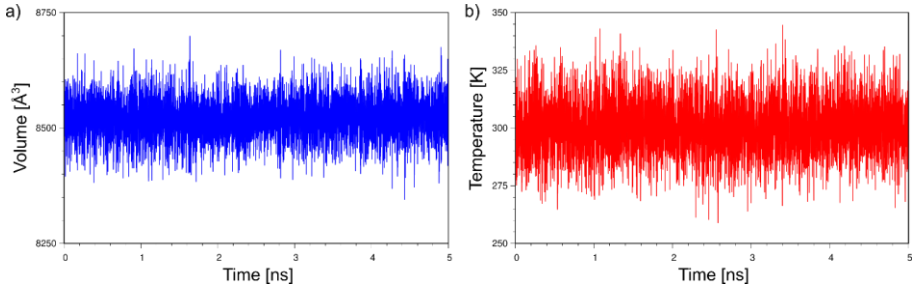

Figure 4A.1. *Panels a and b provide the simulation box volume in Å^3 (blue line) and the simulation temperature in K (red line) along the last 5 ns of classical MD NPT equilibration, respectively.*

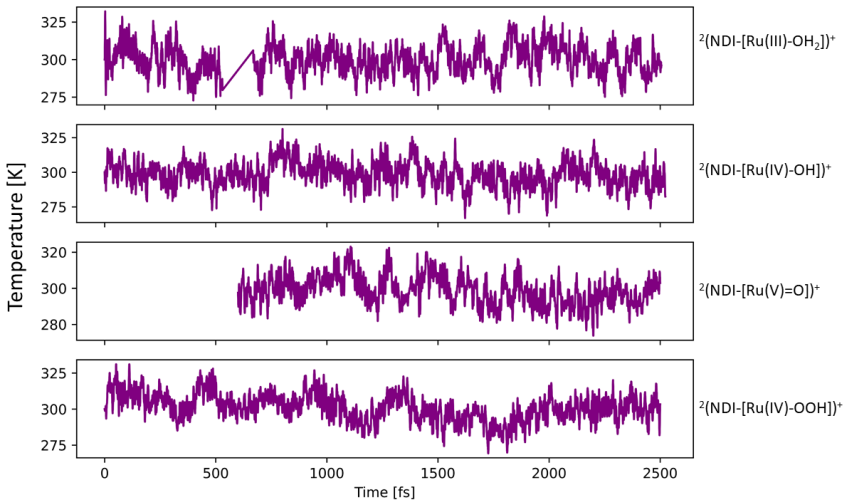

Figure 4A.2. *Temperatures of the equilibration runs at the DFT (PBE) level for the ^{2}(NDI-[Ru(III)-OH$_2$])$^+$, ^{1}(NDI-[Ru(IV)-OH])$^+$, ^{2}(NDI-[Ru(V)=O])$^+$, and ^{1}(NDI-[Ru(IV)-OOH])$^+$ intermediates.*

4A.3 Additional information on the simulations on the ^{2}(NDI-[Ru(III)-OH$_2$])$^+$) complex

4A.3.1 Time evolution of ligand bond distances in ^{2}(NDI-[Ru(III)-OH$_2$])$^+$) complex

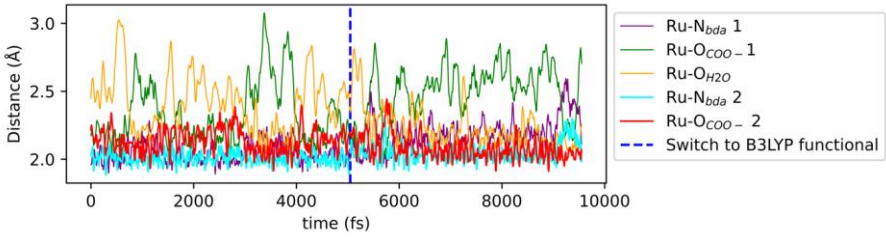

Figure 4A.3. *Time evolution of the bond distances between the ruthenium center, the nitrogen backbone atoms and the carboxylate oxygen atoms of the equatorial bda^{2-} ligand, and the aqua ligand.*

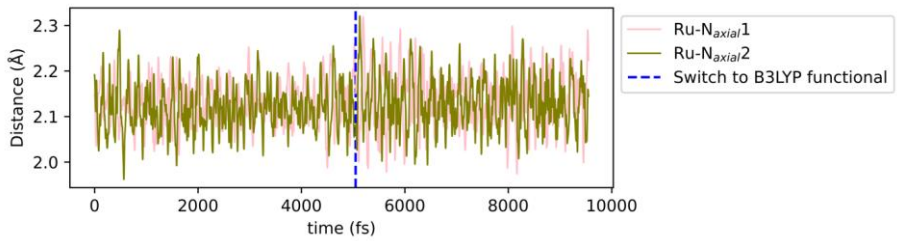

Figure 4A.4. *Time evolution of the bond distances between the ruthenium center and the nitrogen atoms of the axial picoline ligands.*

4A.3.2 First PCET step

The first PCET reaction was simulated at the PBE level of theory. One α-electron was removed from the dye fragment of the molecule, leading to an open-shell-singlet configuration with one unpaired α-electron on the catalyst and one unpaired β-electron on the dye. The spin-densities on the dye and on the catalyst part of the complex as well as the O-H_1 and O-H_2 bond lengths are plotted in Figure 4A.5. Interestingly, the open-shell state was found to form only partially, with a total spin-moment of only 0.4 on the dye and −0.6 on the catalyst and decayed within 50 fs to the closed-shell spin-configuration. A single point energy calculation performed after removing the electron and using tighter SCF convergence criteria converges to an electronic state where the open shell character is almost negligible (<|0.1| Mulliken spin density accumulation on the catalyst and dye fragments of the molecule). This suggests that the reactant and product electronic states are already very close in energy, and this electron transfer step in the catalytic cycle is essentially instantaneous upon oxidation of the dye and does not depend on nuclear rearrangements.

After the electron has transferred to the dye, the resulting Ru^{IV}-bda complex was found reside consistently in a 7-coordinated configuration, where both carboxylate ligands, as well as the aqua ligand bind strongly to the ruthenium and the bond distances are ~2.0 Å. As a response to the oxidation event and binding

of the aqua ligand, the O-H bonds of the ligand are activated, leading to alternating elongations of their respective bond lengths (named O-H_1 and O-H_2 in Figure 4A.5). The dissociated proton remains within close proximity of the hydroxide ligand during the remainder of the simulation, instead of long-range transfer by a Grotthuss mechanism. The fact that the proton does not diffuse further from the hydroxide ligand within the simulated time domain could be due to limited sampling or to finite box size effects.

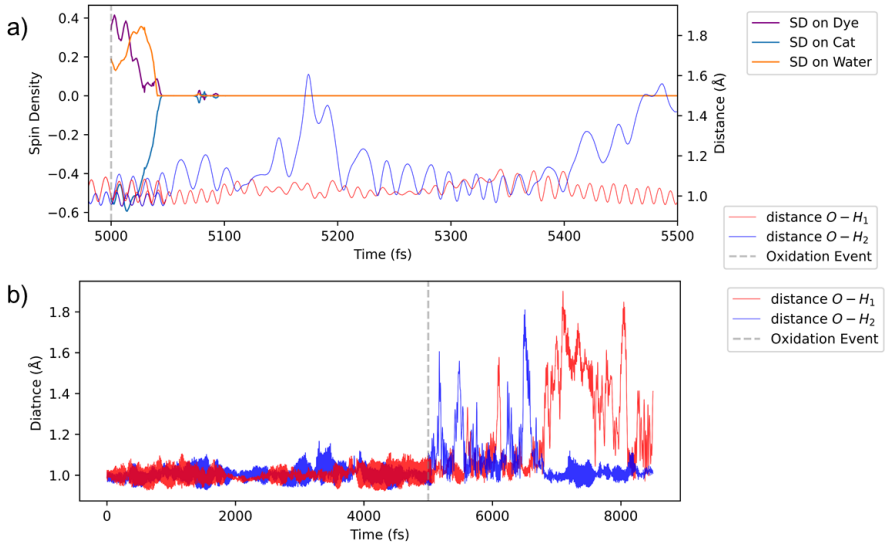

Figure 4A.5. *Panel a provides the time-evolution of the spin-densities (SD) on the catalyst, dye, and water environment, as well as the two O-H bond distances of the aqua ligand for the first 0.5 ps after the oxidation event. The O-H bond distances of the aqua ligand are also plotted in b for the duration of the entire simulation.*

4A.4 Additional information on the simulations of the 1(NDI-[Ru(IV)-OH]+) complex

4A.4.1 The second PCET step

As for the first PCET step, the ^{1}(NDI-[Ru(IV)-OH]$^{+}$) system was equilibrated for 5 ps, where now one proton was removed from the simulation box. At this stage, the complex strongly binds the OH^{-} ligand in a symmetric 7-coordinated environment of the Ru^{IV} ion with $d_{Ru\text{-}O} \approx 1.90$ Å. A strong hydrogen bonding network emerged near the hydroxide ligand, where a nucleophilic water was coordinated to the proton, which was in turn also coordinated by two water molecules (see Figure 4A.7).

The photooxidation process was simulated by removing one electron from the simulation box, now resulting in a doublet ^{2}(NDI$^{\bullet+}$-[Ru(IV)-OH]$^{+}$) species with the unpaired electron found predominantly on the NDI. In Figure 4A.6, the integrated spin density on the dye, catalyst, and water environment are plotted over time in blue, orange, and green respectively. In the same plot, also the length of the dissociating O-H bond is plotted. It is observed that the two quantities evolve in a highly correlated manner, underlining the concerted nature of this PCET step. The photoexcited state was found to live significantly longer in the second PCET step than for the first PCET step, indicating that the electronic state in which the dye is oxidized, and not the ruthenium, does present a minimum on the potential energy surface in this catalytic step. Completion of the electron transfer from the Ru^{IV}-bda complex to the dye was observed in ~400 fs. Immdiately after removal of the electron on the dye, some spin density on the catalyst has already recombined with the excess hole density on the NDI. Also, a significant fraction was found to delocalize on the water environment. This was also observed for the first PCET step. Given the tendency of GGA-functionals to overemphasize charge delocalization, it was decided to replicate this PCET step at the B3LYP level of theory.[3–6] Contrarily to the simulations with the PBE functional, the excess spin localized exclusively on the dye component of the

complex post-oxidation, as depicted in Figure 4A.6, panels b and c. The system was observed to remain in the reactant state for the duration of 2.5 ps, without undergoing a spontaneous PCET event. To obtain a reactive trajectory, Metadynamics (metaD) was used, as implemented in the Plumed library. A constant bias potential characterized by a height of 0.621 kcal mol^{-1} and width 0.1 Å, was deposited every 10 fs, acting along a collective variable defined by the dissociating O-H bond distance. Interestingly, the electron transfer event was observed to unfold on an ultrashort timescale, with the total spin density on the dye transferring to the catalyst within a few femtoseconds. This observation aligns with the expectation that in Born-Oppenheimer molecular dynamics simulations, the electronic system remains strictly quenched to the absolute ground state. In previous work, we have shown that the electron transfer in this catalyst-dye system can be described by two electronic states that cross along the proton transfer reaction coordinate.[7] The proton and electron dynamics in this PCET event are strongly coupled, as it is observed that the electron transfer takes place as soon as the dissociating O-H bond is elongated to about ~1.4 Å. Due to the aggressive biasing, it is not meaningful to analyze the obtained free energy surface associated with the MetaD simulation.

In summary, a GGA-based simulation predicted the PCET event to occur spontaneously, while the hybrid-functional-based simulation does not show this event on the few picoseconds timescale. This observation aligns with benchmark tests that show that GGA functionals consistently underestimate proton transfer barriers in water by about 3 to 3.5 kcal mol^{-1}.[8] Based on previous work in our group, we expect the GGA-DFT predicted barrier for ruthenium-catalyzed oxidation of the hydroxide ligand to be of the order of 2 kcal mol^{-1}.[9] With hybrid functionals this would thus increase to ~5 kcal mol^{-1}. Therefore, the apparent discrepancy between the GGA and hybrid-DFT simulations can be attributed to the difference in the predicted activation barriers.

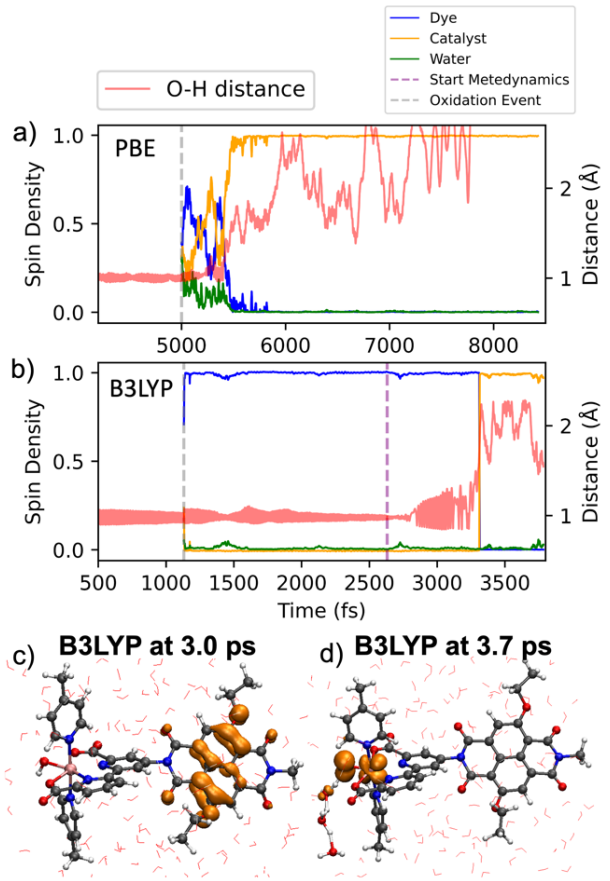

Figure 4A.6. *The evolution of the spin density on the dye (blue), catalyst (yellow), and water (green) components of the system are plotted over time as calculated with the PBE functional (a) and with the B3LYP functional (b). The dissociation O-H bond lengths are plotted in red. In the simulations with the B3LYP functional, the spin densities are localized exclusively on the dye and on the catalyst, whereas with the PBE functional the spin density is delocalized significantly on the water. The oxidation event is indicated with a vertical dashed line in both figures. The vertical purple dashed line in b indicates the moment from which bias potentials were deposited. Figures c) and d) provide a visualization of the spin density right before and after the PCET event in the simulation performed with the B3LYP functional.*

4A.4.2 Manifestation of a hydrogen bonding network around the 1(NDI-[Ru(IV)-OH]+) intermediate

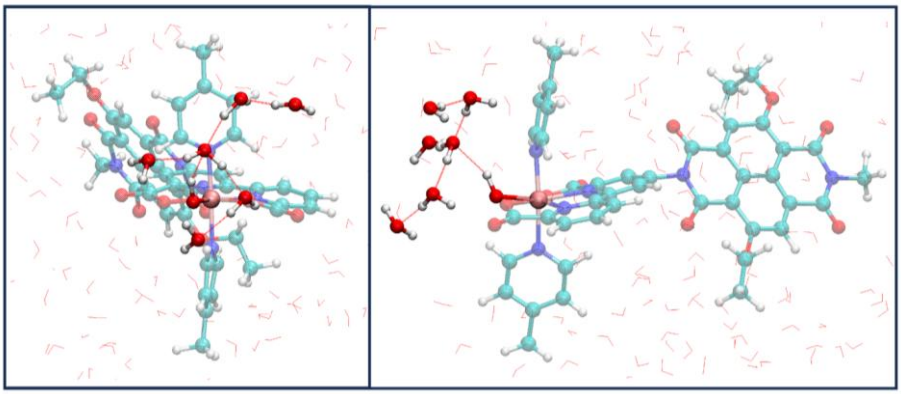

Figure 4A.7. *Front- (left) and side-view (right) of the hydrogen bonding network that form around the hydroxide ligand during the equilibration run of the* ^{1}*(NDI-[Ru(IV)-OH]*$^{+}$*) intermediate.*

4A.5 Spin-densities of ^{2}(NDI-[Ru(III)-OH$_2$]$^{+}$), ^{2}(NDI-[Ru(V)=O]$^{+}$) and ^{2}(NDI$^{+\bullet}$-[Ru(V)=O]$^{+}$) intermediates

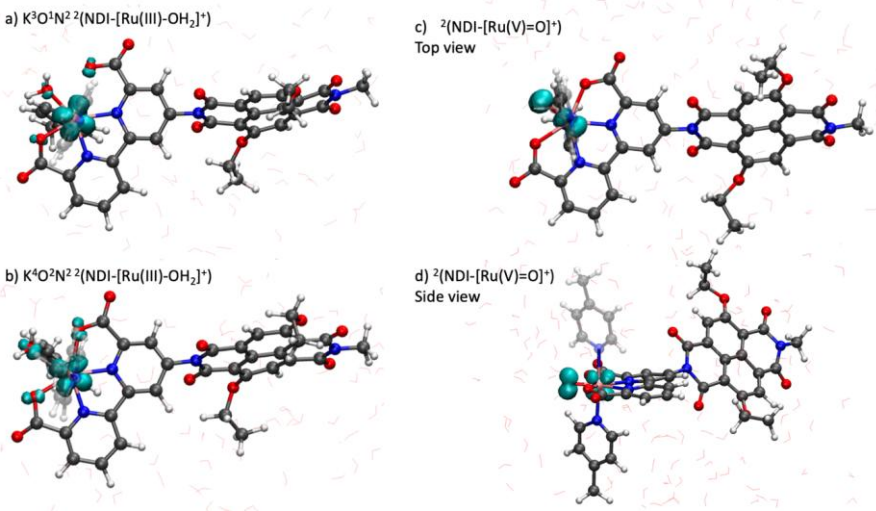

Figure 4A.8. *Spin-densities on the* ^{2}*(NDI-[Ru(III)-OH$_2$]$^{+}$) (a and b) and* ^{2}*(NDI-[Ru(V)=O]*$^{+}$*) intermediates (c and d).*

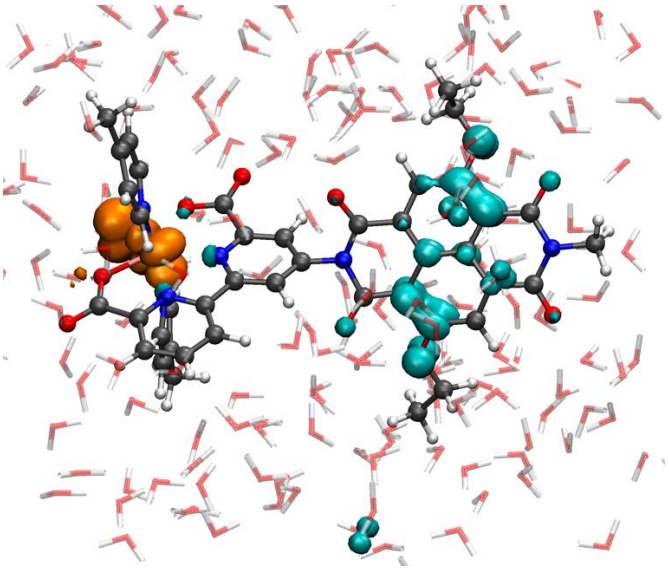

Figure 4A.9. *Spin-density on the* ^{2}(NDI$^{+\bullet}$-[Ru(V)=O]$^{+}$) intermediate.

4A.6 Enhanced sampling methods to accelerate the rate determining O-O formation step

4A.6.1 Metadynamics Simulations of O-O bond formation

As collective variable (CV), the O-O distance between the oxo ligand and the nearest water molecule in the solvent shell was chosen.[3,12] A quadratic wall was employed at a CV value of 3.1 Å to restrict the explorable configuration space to a minimum by preventing the nucleophilic water molecule from drifting away. The initial bias with a height 0.5 kcal mol^{-1} and width of 0.1 Å was adaptively scaled during the simulation based on a target bias factor of 35 $k_{B}T$. After 22.7 ps, the initial bias height had decreased to about ~0.15 kcal mol^{-1}, while the fluctuations in the collective variable did not yet get close to a transition, which we expected to be around 1.75 Å. At that point, it was decided to continue the simulation with a constant Gaussian height of 0.2 kcal mol^{-1}. The Gaussians were deposited along the CV every 50 fs. The Metadynamics simulation terminated

after the first crossing event, which took place after 31.0 ps. This is justifiable since the purpose of this study was to investigate the activation barrier and mechanism for the PCET step in question and not the free energy difference between the reactant and product states.

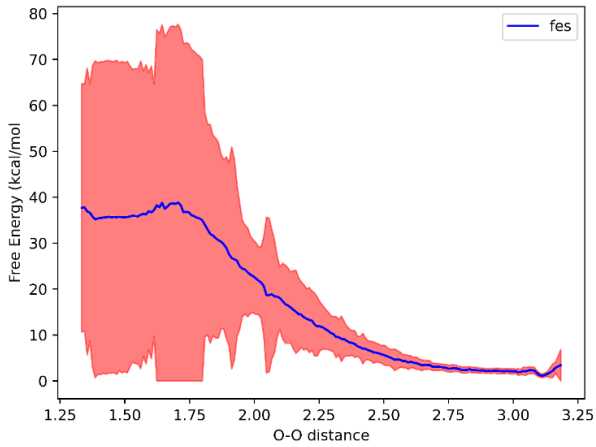

Figure 4A.10. *Plot of the free energy profile obtained from the Metadynamics simulations (blue) performed at the GGA-PBE level of theory. The total simulation time amounted to ~31 ps. The error (1 standard deviation) for the free energy is given in the red shaded area. The barrier of O-O bond formation was found to amount to ~40 kcal* mol^{-1}*. The high uncertainty in the obtained free energy profile indicates that a considerably longer simulation needs to be carried out to obtain a converged result.*

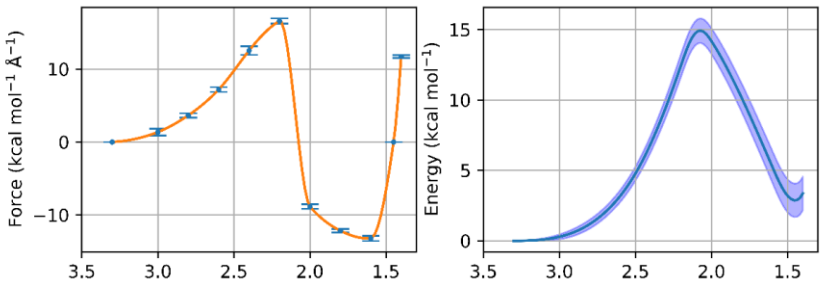

Figure 4A.11. *FES calculated at the PBE-level, plotted as a function of the O-O distance reaction coordinate. The free energy was obtained by thermodynamic integration of a 100-point Akima spline fit of the averaged constraint forces, $<\lambda>$, at different values of the O-O bond distance. The error bars on $<\lambda>$ are obtained by block averaging. The error on the FES is calculated by integrating the upper and lower bounds of the $<\lambda>$ profile.*

4A.6.2 Blue moon simulations of O-O bond formation

The Blue Moon Ensemble Free energy profile was constructed from nine AIMD simulations performed with a constrained O-O distance of 3.0, 2.8, 2.6, 2.4, 2.2, 2.0, 1.8, 1.6 and 1.4 Å. In addition, simulations in the reactant and product states were performed to determine the equilibrium O-O bond lengths. The average bond length in the product state was found to fluctuate around 1.45 Å. To improve the FES integral quality, an additional point was added on the *y*-axis at an *x*-value of 1.45 Å. The radial distribution function of the oxo-ligand with all oxygen atoms of the solvent water molecules is plotted in Figure 4A.12. The data for this figure were extracted from the 2.5 ps equilibration of the open-shell singlet state. It is observed that the function reaches its first maximum in the range from 3.3 to 4.0. It was, therefore, decided to add another point in the force profile at 3.3 Å. The final free energy profile was obtained by thermodynamic integration of a 100-point Akima spline interpolation of the mean forces along the reaction path.

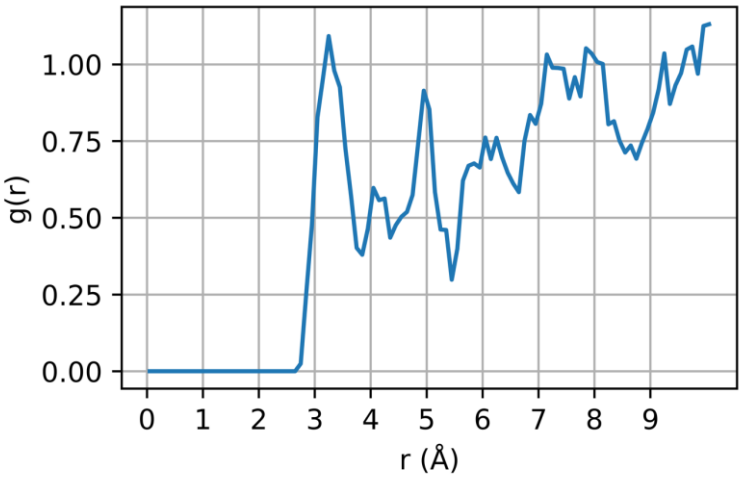

Figure 4A.12. *Radial pair distribution function, g(r), of the oxo ligand with all solvent water oxygen atoms.* The distance *r* is given in *Å*.

Plots of the temperature during the constrained AIMD simulations are provided in Figure 4A.13 for the PBE simulations. It is observed that all simulations equilibrated within 0.5 ps. Figure 4A.14 provides a plot of the temperature evolution in the B3LYP simulations, which appear to be properly equilibrated from the start. The time evolutions of the constraint forces are plotted in Figure 4A.15 (PBE) and Figure 4A.16 (B3LYP), as well as the running average which culminates in the mean force for each specific run.

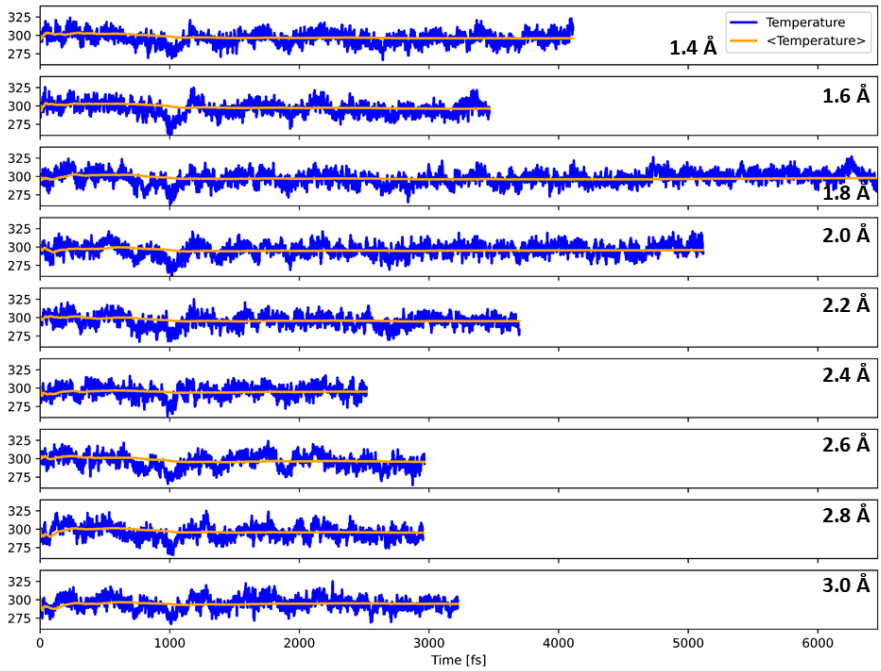

Figure 4A.13. *Temperature evolution during Blue Moon ensemble simulations (PBE) of the* $^{1}(NDI^{+\bullet}\text{-}[Ru(V)=O]^{+})$ *intermediate and an* H_2O *molecule with constrained intramolecular O-O distances.*

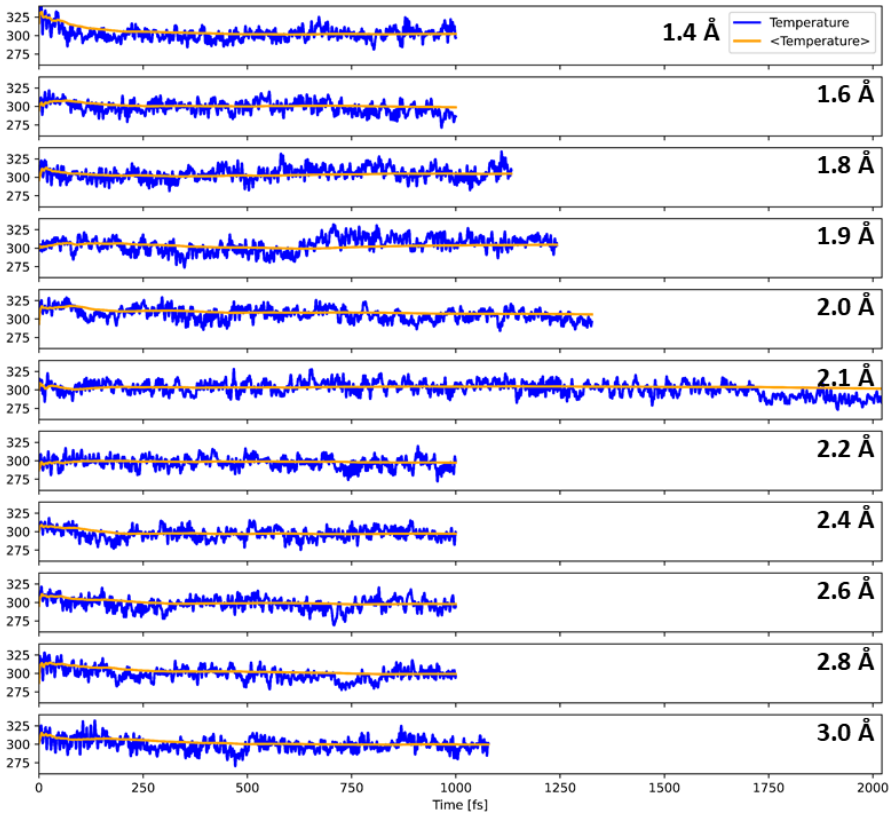

Figure 4A.14. *Temperature evolution during Blue Moon ensemble simulations (B3LYP) of the* $^{1}(NDI^{+}\bullet\text{-}[Ru(V)=O]^{+})$ *intermediate and an* H_2O *molecule with constrained intramolecular O-O distances.*

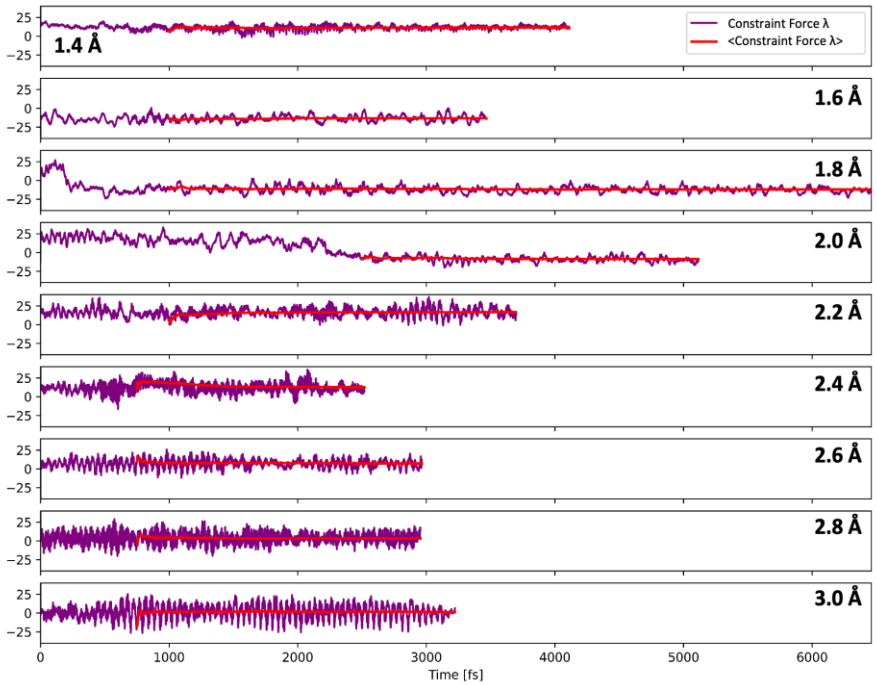

Figure 4A.15. *Constraint force evolution during Blue Moon ensemble simulations (PBE) of the* $^{1}(NDI^{+}\bullet\text{-}[Ru(V)=O]^{+})$ *intermediate and an* H_2O *molecule with constrained intramolecular O-O distances.*

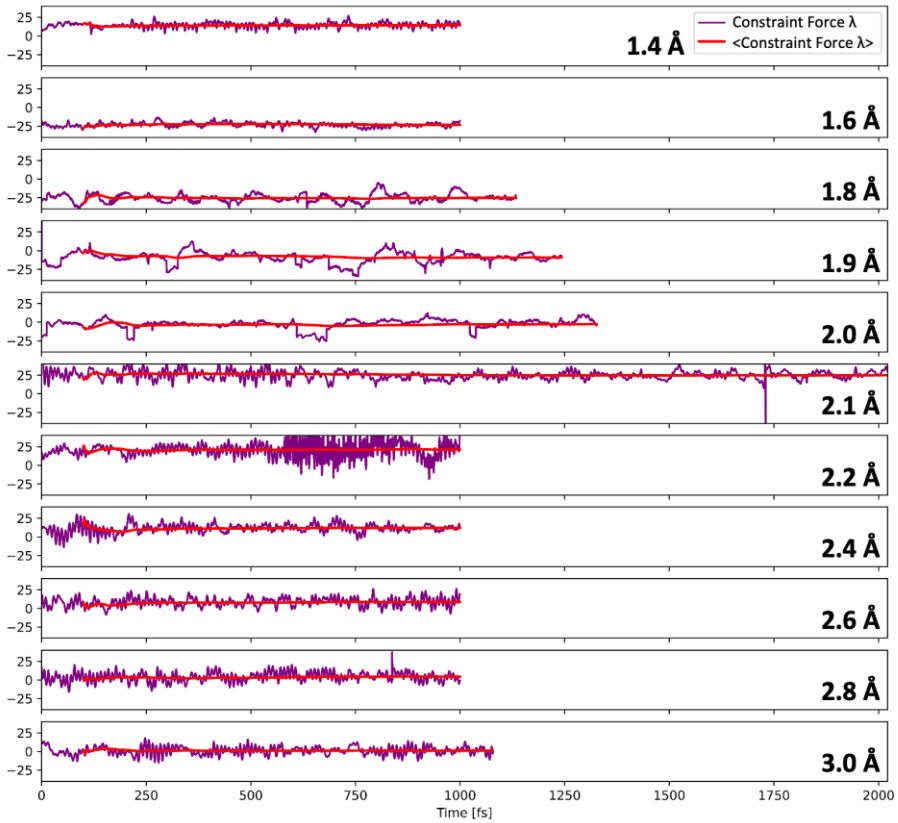

Figure 4A.16. *Constraint force evolution during Blue Moon ensemble simulations (B3LYP) of the* ^{1}*(NDI*$^{+}$*•-[Ru(V)=O]*$^{+}$*) intermediate and an* H_2O *molecule with constrained intramolecular O-O distances.*

4A.6.3 Estimation of error bars using block averaging

To reduce the time correlation effects in the error estimate of the mean forces, the total trajectory was cut in blocks. The error was then estimated as one standard deviation in the averaged constrain force values among all blocks:

$$\sigma = \sqrt{\frac{1}{N}\sum_{i=1}^{N}(x_i - \mu)^2}$$

Where i runs over the block indexes, N is the total number of blocks, x_i is the λ average of the block, and μ is the mean λ over all blocks.

In Figure 4A.17 (PBE) and A18 (B3LYP), the calculated error is plotted as a function of the block size for all simulations. Due to time correlations, the errors initially increase steeply with the block size, however, when the block size increases to ~100 time steps, the errors plateau. Most of the calculations display some noise in the error estimates with larger block sizes, which can be attributed to the decreasing number of blocks at that stage. Nevertheless, all error estimates appear to converge within the given simulation time, and the error bar estimates were extracted by taking the maximum value running average of the error.

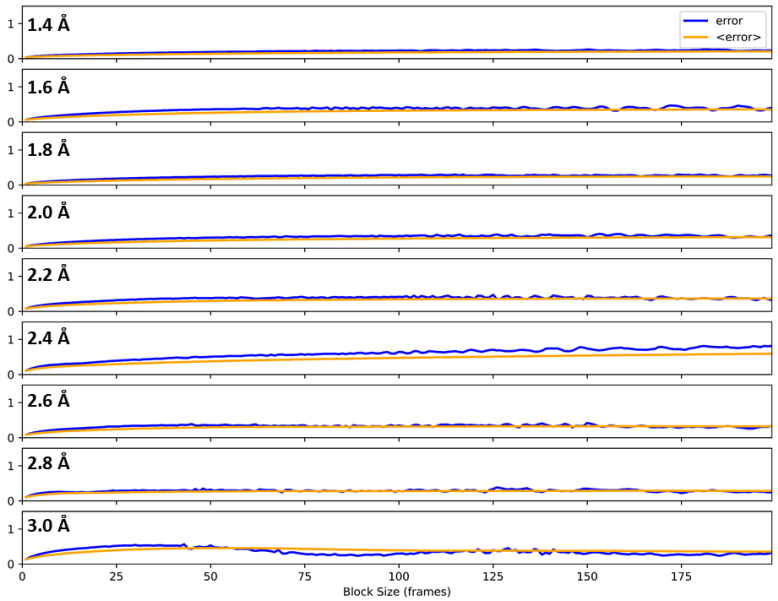

Figure 4A.17. *Convergence of the mean force error with increasing block lengths for the different constrained simulations (PBE). The error is quantified as one standard deviation in the value of λ calculated between different blocks.*

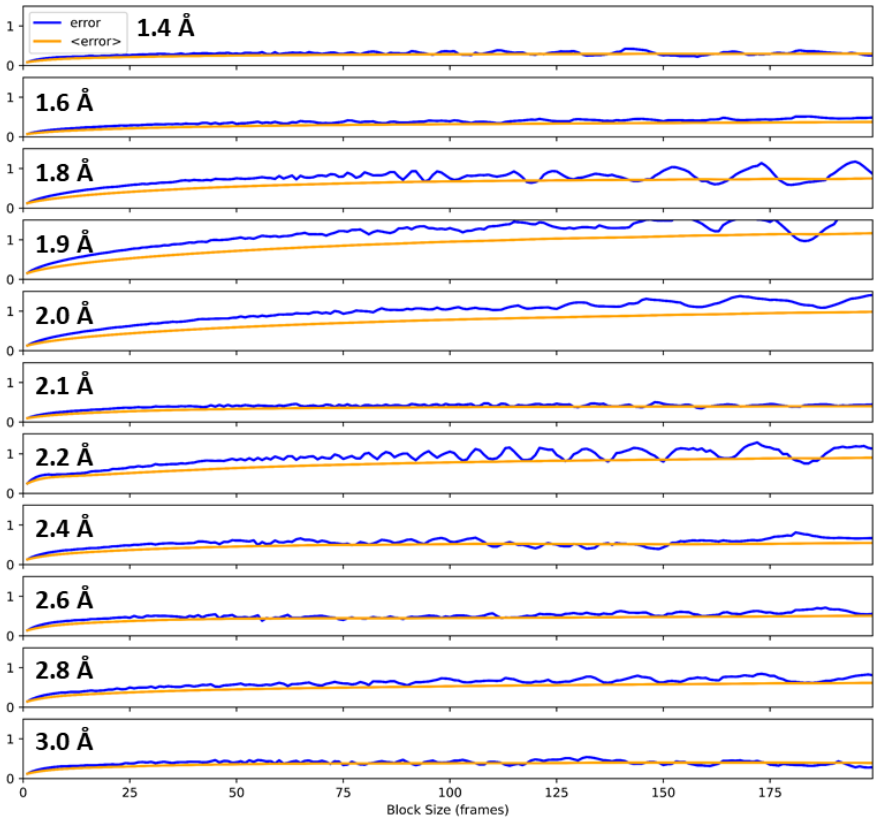

Figure 4A.18. *Convergence of the mean force error with increasing block lengths for the different constrained simulations (B3LYP). The error is quantified as one standard deviation in the value of λ calculated between different blocks.*

4A.7 Level of theory benchmarks

To justify the applied level of theory, several benchmark studies were performed. The first benchmark involved geometry optimization of the ^{1}(NDI-[Ru(IV)-OH])$^{+}$ and ^{1}(NDI$^{\bullet+}$-[Ru(V)=O])$^{2+}$ intermediates. The calculations were performed at four different levels of theory, which are outlined in Table 4A.1. The geometry optimizations were carried out with convergence criteria of $1{\cdot}10^{-4}$ Hartree Bohr^{-1} and $5{\cdot}10^{-5}$ Hartree Bohr^{-1} for the max and RMS changes in the forces, and $1{\cdot}10^{-4}$ Bohr and $5{\cdot}10^{-5}$ Bohr for the max and RMS changes in the atomic displacements. A similar test has been carried out by Meijer and coworkers, who found that the

geometry of a similar ruthenium based water oxidation catalyst was properly described with the DZVP basis in conjunction with a plane wave cut-off of 280 Ry.[10] After the optimization, we compared the bond distances from the Ru center to all atoms in the first coordination sphere. For the $^{1}(NDI^{\bullet+}\text{-}[Ru(V)=O])^{2+}$ intermediate, we investigated also the Mulliken spin accumulation on the combined Ruthenium atom and oxo ligand. The investigated bond distances for the $^{1}(NDI\text{-}[Ru(IV)\text{-}OH])^{+}$ complex are provided in Table 4A.2, while the investigated bond distances and Mulliken spin accumulations for the $^{1}(NDI^{\bullet+}\text{-}[Ru(V)=O])^{2+}$ complex are provided in Table 4A.3.

Table 4A.1. The four different sets of numerical parameters that were benchmarked.

	GGA lower setting	GGA higher setting	Hybrid lower setting	Hybrid higher setting
Functional	PBE	PBE	B3LYP	B3LYP
Gaussian basis	DZVP-MOLOPT-GTH[a]	TZVP-MOLOPT-GTH[a]	DZVP-MOLOPT-GTH[a]	TZVP-MOLOPT-GTH[a]
PW basis	280Ry	400Ry	280Ry	400Ry
EPS Schwartz	-	-	10E–6	10E–8
ADMM basis	-	-	cFIT3[b]	pFIT3[b]

[a] In all cases the DZVP-SR-MOLOPT-GTH basis was employed for ruthenium, as no larger basis was available.

[b] For ruthenium the cFIT11 and FIT11 ADMM basis sets were used for the low and high settings calculations, respectively.

Table 4A.2. Comparison of coordination bond lengths to Ru(IV)-OH intermediate computed at different levels of theory. See Figure 4A.19. a) for the atomic labeling in the Ru complex.

	GGA lower setting	GGA higher setting	Hybrid lower setting	Hybrid higher setting	Experiment [11] Ru(IV)-OH
Ru-N_{bda} 1	2.13	2.12	2.16	2.17	2.09
Ru-N_{bda} 2	2.13	2.13	2.17	2.17	2.09
Ru-O_{coo-} 1	2.10	2.10	2.10	2.11	2.04
Ru-O_{coo-} 2	2.09	2.08	2.06	2.08	2.03
Ru-N_{pic} 1	2.11	2.11	2.11	2.11	2.08
Ru-N_{pic} 2	2.10	2.10	2.10	2.11	2.08
Ru-O_{OH}	1.93	1.93	1.92	1.91	1.96

Table 4A.3. Comparison of coordination bond lengths to Ru(V)=O computed at different levels of theory. See Figure 4A.19. a) for the atomic labeling in the Ru complex.

	GGA lower setting	GGA higher setting	Hybrid lower setting	Hybrid higher setting	Experiment[12] Ru(V)=O
Ru-N_{bda} 1	2.27	2.27	2.29	2.30	~2.1 Å
Ru-N_{bda} 2	2.26	2.26	2.28	2.30	~2.1 Å
Ru-O_{coo-} 1	2.15	2.15	2.16	2.14	~2.1 Å
Ru-O_{coo-} 2	2.13	2.13	2.11	2.13	~2.1 Å
Ru-N_{pic} 1	2.12	2.12	2.13	2.12	~2.1 Å
Ru-N_{pic} 2	2.12	2.12	2.12	2.12	~2.1 Å
Ru-O_{oxo}	1.70	1.70	1.70	1.70	1.75±0.02 Å
Spin Moment on Ru(V)=O	0.744	0.748	1.047	1.045	-

Table 4A.2 shows that the investigated bond distances are in close agreement with the available X-ray data of the $[(bda)(pic)_2Ru(IV)\text{-}OH]^+$ complex. Minor differences, on the order of 0.05 Å, may arise from covalent binding of the NDI-dye to the bda^{2-} backbone, intrinsic DFT errors or limited X-ray resolution.

Importantly, the overall trends in bond lengths within the $^1(NDI\text{-}[Ru(IV)\text{-}OH])^+$ complex are reproduced, including the shortening of the Ru-O bond distance from ~1.96 in Ru(IV)-OH to ~1.75 Å in Ru(V)=O. Increasing the computational settings did not significantly affect the Mulliken spin accumulation on the Ru(V)=O intermediate, although a difference between functionals is observed. Overall, this test thus shows that accurate structural and electronic properties are produced with a Gaussian basis of DZVP quality, in conjunction with a plane wave basis with a cutoff of 280 Ry.

The second benchmark involved DFT-MD simulations of the $^1(NDI^{\bullet+}\text{-}[Ru(V)=O])^{2+}$ intermediate. All benchmark DFT-MD simulations were equilibrated for 300 fs and subsequently propagated for another ~0.5 to 1 ps. To verify the quality of the performed MD simulations, we computed the oxygen-oxygen radial pair distribution function (RDF). The RDF's obtained at the different levels of theory are displayed in Figure 4A.19b. We do not observe significant changes between the RDF's computed at various levels of theory, further validating the level of theory employed in this paper.

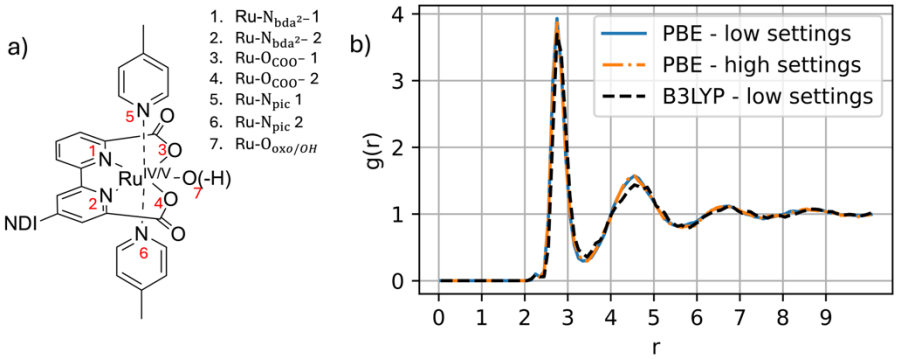

Figure 4A.19. *a) Schematic structure and atomic labeling of the Ru complex; b) O-O radial distribution function computed from molecular dynamics simulation with PBE/DZVP+280Ry (blue), PBE/TZVP+400Ry (red) and B3LYP/DZVP/+280Ry (black). The distance r is given in Å.*

4A.8 References

[1] H. Eyring, *J. Chem. Phys.* **1935**, *3*, 107–115.
[2] E. Pollak, P. Talkner, *Chaos* **2005**, *15*, 026116.
[3] J. Cheng, M. Sulpizi, J. VandeVondele, M. Sprik, *ChemCatChem* **2012**, *4*, 636–640.
[4] Aron J. Cohen, Paula Mori-Sánches, Weitao Yang, *Science* **2008**, *321*, 792–794.
[5] C. Li, X. Zheng, N. Q. Su, W. Yang, *Natl. Sci. Rev.* **2018**, *5*, 203–215.
[6] K. R. Bryenton, A. A. Adeleke, S. G. Dale, E. R. Johnson, *Wiley Interdiscip. Rev. Comput. Mol. Sci.* **2023**, *13*, e1631.
[7] T. de Haas, H. van Overeem, H. J. M. de Groot, F. Buda, *ChemPhotoChem* **2023**, e202200274.
[8] A. Hassanali, F. Giberti, J. Cuny, T. D. Kühne, M. Parrinello, *Proc. Natl. Acad. Sci. U.S.A.* **2013**, *110*, 13723–13728.
[9] Y. Shao, J. M. De Ruiter, H. J. M. De Groot, F. Buda, *J. Phys. Chem. C.* **2019**, *123*, 21403–21414.
[10] N. Govindarajan, A. Tiwari, B. Ensing, E. J. Meijer, *Inorg. Chem.* **2018**, *57*, 13063–13066.
[11] L. Duan, A. Fischer, Y. Xu, L. Sun, *J. Am. Chem. Soc.* **2009**, *131*, 10397–10399.
[12] D. Lebedev, Y. Pineda-Galvan, Y. Tokimaru, A. Fedorov, N. Kaeffer, C. Copéret, Y. Pushkar, *J. Am. Chem. Soc.* **2018**, *140*, 451–458.